UC Berkeley
UC Berkeley Electronic Theses and Dissertations

Title
Developing Laboratory Seismic Inversions

Permalink
https://escholarship.org/uc/item/2kd2s6fx

Author
Parker, Jes

Publication Date
2022

Peer reviewed|Thesis/dissertation

eScholarship.org Powered by the California Digital Library
University of California

Developing Laboratory Seismic Inversions

by

Jes Morrison Parker

A dissertation submitted in partial satisfaction of the

requirements for the degree of

Doctor of Philosophy

in

Engineering - Civil and Environmental Engineering

in the

Graduate Division

of the

University of California, Berkeley

Committee in charge:

Professor Kenichi Soga, Chair
Professor Douglas Dreger
Professor Sanjay Govindjee

Spring 2022

Developing Laboratory Seismic Inversions

Copyright 2022
by
Jes Morrison Parker

Abstract

Developing Laboratory Seismic Inversions

by

Jes Morrison Parker

Doctor of Philosophy in Engineering - Civil and Environmental Engineering

University of California, Berkeley

Professor Kenichi Soga, Chair

Earthquakes are simulated in the laboratory using a homogeneous rock analog material, taking advantage of highly controlled conditions to investigate the source properties of asperity rupture. The frictional interface consists of two transparent Poly(methyl-methacrylate) (PMMA) blocks with self-similar roughness profiles imposed by sand blasting and laser engraving to match our understanding of rock-rock interfaces. The resulting interface is imaged by a pressure sensitive film revealing the real contact area spread over sparsely distributed 1 mm patches called asperities. Stick slip events on the direct shear fault are recorded by an array of absolutely calibrated, single component displacement acoustic emissions (AE) sensors. Rupture events which are fully contained within the fault surface have radiation patterns consistent with double couple source mechanisms aligned with the fault plane and strike, making them earthquake-like events at the millimeter scale. A catalog is developed containing 50 Mw-7.5 to Mw-6.5 events which exhibit self-similar scaling properties in estimated magnitude and rupture area, which connects these events to previously observed earthquake scaling behavior at laboratory and natural scales.

The acoustic emissions sensors are absolutely calibrated by a method combining well characterized, broadband calibration sources with a Green's function model for wave propagation through the PMMA base plate. The Green's functions are carefully tuned for the sample-specific material properties of the plate, including anelastic attenuation. Each sensor is individually calibrated and found to have a sensitivity on the order of 1 V/nm. Displacement records for the experimental stick-slip events have sudden onsets, with first arriving pulses around 0.01 - 1 nm in amplitude and 1 - 4 μs in duration. The arrival pulses are often complex in shape, such as having two peaks rather than one smooth pulse. Displacement arrival pulses are directly proportional to the moment-rate function which describes the distribution of slip during the event source. Furthermore, the magnitude analysis of the events indicates a rupture area at the appropriate scale but generally larger than any one asperity observed on the fault surface. Together, these observations indicate that rupture

events recorded likely have coseismic slip spreading over multiple nearby asperities.

In order to study the complex, multiple-asperity sources, a finite source inversion method following Hartzell and Heaton [1] is developed. The method is tested on forward modeled synthetic asperity ruptures, beginning with simple ruptures on single, circular asperity models. Although a brief attempt is made at applying the method to recorded experimental data, more testing and sensitivity analysis is required before the method may be reliably used. Continued work in laboratory scale seismic inversions shows great promise in providing a highly controlled environment for detailed source study of earthquake-like events.

Contents

List of Figures

List of Tables

Acknowledgments

I would like to express my deepest appreciation for Professors Douglas Dreger and Kenichi Soga—without the structured guidance, regular reassuring check-ins, and listening ear they each provided I would never have completed this dissertation. I am extremely grateful to Professor Soga for stepping up to the role of Chair in the last year of my work and guiding me through the writing process. Words cannot express my gratitude to Professor Dreger for the countless technical conversations sharing both invaluable depth of knowledge and contagious excitement for the research material. Special thanks to Professor Sanjay Govindjee for demystifying tensor math and solid mechanics before I knew how well that exposure would serve me and for guidance when I repeatedly found my way to material science questions.

Thanks must also go to numerous individuals and communities that each provided a nourishing combination of professional development and friendship. Thank you to my ACES and CAC communities for chances to feel both more whole and a part of something greater. Many thanks to my USF Engineering community—particularly to Hana, Julia, and Genna—for the chance to experience and contribute to engineering education from a new angle and for their kind and encouraging mentorship. Thank you to my collaborator turned confidant, Tom Smart, for enriching my work environment with friendship and helping me learn the value in forging new connections.

I am grateful to Professor Steven Glaser for the opportunity to pursue graduate studies and access to state-of-the-art laboratory facilities. I would like to extend thanks as well to Paul Selvadurai for early advice and introductions to the work and lab. Special thanks to Professor Robert Herrmann and Professor Greg McLaskey for help calculating Green's functions with Computer Programs in Seismology and the MATLAB implementation of PlateSoln, respectively.

I am grateful that parts of this work were supported by the Department of Defense (DoD) through the National Defense Science & Engineering Graduate Fellowship (NDSEG), the University of California, Berkeley through the Jane Lewis Fellowship, and grants through the National Science Foundation (CMMI-1131582, CMMI-1650964).

Finally, I would like to thank those close to me for personal support throughout my life that enabled me to pursue this accomplishment. I am forever grateful to my parents, Mike and Marla, for modeling and encouraging unending curiosity and delight in seeking to understand the world around me, as well as their unwavering love and support. Thanks and love to my partner, Sorren, for being my rock and to my brother, Nick, for always having a story to tell me. My deepest gratitude to all five of my grandparents for their dedicated lifetimes of work building the family that raised and supported me. Thank you to the grandfathers I lost during grad school, Larry and Paul, for letting me know how proud they were of me and thank you to my grandmothers, Mary and Esther, for their delightful companionship and reminders of all the joys yet to come. Thank you to the therapists who helped me find and stay true to my way during a compoundly complex period of my life. Thank you to all of the other friends and family who have been there for me leading up to and

throughout these years. Last but not least, thank you to my cat Toast, for dutifully trapping me at my desk with a warm lap and never catastrophically stepping on my keyboard.

Chapter 1

Introduction and Literature Review

1.1 Introduction

Understanding the mechanics of faulting and the dynamics of earthquake rupture is crucial to better characterizing fault behavior and earthquake hazard. In this thesis laboratory scale friction is explored through a direct shear experiment and the source parameters of the nano-earthquakes observed are investigated. This work iterates on an existing base of laboratory and strong-motion seismic methods and understanding in pursuit of a detailed kinematic and dynamic source study of individual laboratory stick-slip events.

In the next section a literature review of key elements to the research is presented. Chapter 2 describes the many elements of the experimental setup and modeling. The physical direct shear apparatus and load system are presented, followed by the choice of a wave propagation model through the base plate. Acoustic emissions sensors which record local displacements are calibrated and the calibration sources are used to confirm the consistency of the full system model. Chapter 3 includes early efforts in applying a finite source inversion method to laboratory scale events. Simple synthesized sources are used to begin an investigation of the inversion requirements. Attempts at applying the early finite source inversion algorithm to recorded event data revealed that the basic seismic analysis of the events—necessary for comparison of the finite source results—was insufficient. Chapter 4 includes a detailed analysis of the seismicity produced by the experiment, from event detection to a magnitude and scaling analysis of the resulting event catalog. The acoustic emissions events observed match the expected source and scaling properties for seismic events at all observed scales. In Chapter 5 the results and recommendations for future work are summarized.

1.2 Laboratory Seismology

Brace and Byerlee [2] linked the stick-slip behavior observed on rock faults in the laboratory to Reid's elastic rebound theory of earthquake mechanisms—the first description of radiated earthquake energy as the result of a sudden release of shear strain. The Reid theory

[3] proposed that the energy released in an earthquake was due to the sudden fracture of originally intact rock. Researchers in the following decades had difficulty reconciling this fracturing mechanism with the the observed stress drop, which was much lower than the strength of relevant earth materials. Brace and Byerlee [2] loaded a granite cylinder in a triaxial machine with increasing axial stress until it fractured, then continued to apply load and observed stick slip behavior. Subsequent slips were accompanied by stress drops much smaller than the original fracture strength and a sawcut specimen displayed similar behavior. From these and related experiments they concluded that stick slip motion in already fractured rock could provide an earthquake mechanism that integrated Reid's theory of sudden strain release with the low stress drop observations. In response to other contemporary laboratory shear experiments that demonstrated smooth rather than stick slip sliding for different load and temperature conditions, Brace and Byerlee [2] cited work with stick slip friction in engineering materials that exhibited strong dependence on the characteristics of the machine used to apply the shear load.

The rate and state frictional laws described by Dieterich [4] and Rice and Ruina [5] used empirical data from rock friction experiments to formulate constitutive relationships that, combined with the stiffness of the load machine, controlled the observed stick slip behavior. Dieterich [4] conducted direct shear experiments in granodiorite ground to three different roughnesses and focused on simulating the observed frictional strength under varied load and slip conditions. His results showed dependency on slip rate and fault displacement, controlling age of contacts. Rice and Ruina [5] abstracted the displacement dependency to a fault state that evolves in time, leading to the rate and state terminology. They produced complex mathematical models linked to simplified mechanical models and surveyed the large variety of potential slip conditions that can occur within the rate and state parameter space. Although the rate and state laws have remain relevant to laboratory study of friction, they are a purely phenomenological model and provide little insight toward the underlying contact mechanics and source physics of stick-slip events [6].

Specific study of the energy radiated from stick-slip events as stress waves is achieved in the laboratory by recording acoustic emissions. Lockner [7] summarized the emerging field of acoustic emissions studies of stick-slip events as analagous to seismic studies of earthquake phenomena. Laboratory events were shown to adhere to the frequency-magnitude relationships governing the overall prevalence of stick-slip events—the Gutenberg-Richter law—and the cluster-specific decay of aftershock frequency—the Omori law. Relatively small magnitude events called foreshocks occur prior to the largest stick-slip events sustained by the interface, which are regarded as main shocks.

Laboratory earthquake observations have also entered into the long-standing question of self-similar earthquake scaling. Kanamori and Anderson [8] identified a log-linear relationship between fault area and seismic moment, which indicates a constant stress drop. They analyzed large earthquakes with seismic moments ranging from 10^{17} Nm to 10^{23} (Mw 6-9). Later work by Mayeda and Walter [9] using events ranging from Mw2.2-7.3 reported a strong dependency between stress drop and moment, with the stress drop proportional to $M_0^{0.25}$. Nadeau and Johnson [10] studied a well-established and recorded repeating event at

Parkfield and observed the opposite—stress drop decreasing with increasing moment. Laboratory studies have contributed both in observations consistent with constant stress drop self-similar scaling and in possible mechanisms for breaking self-similarity. Goodfellow et al. [11] used laboratory-scale events recorded in situ by acoustic emissions sensors enclosing a rock sample within a tunnel wall at the Underground Research Laboratory. They produced a summary figure (included in Fig. 4.8) demonstrating the observed self-similar scaling and contextualizing their results with other laboratory and natural seismicity spanning 20 orders of magnitude in seismic moment. However, Malagnini et al. [12] studying crustal earthquakes observed both increasing stress drop with increasing moment and a high-stress-drop asymptote for large events, citing laboratory results from high-speed rock experiments presented by Di Toro et al. [13] as support for frictional weakening and lubrication mechanisms producing the asymptotically increasing behavior. Ide and Beroza [14] suggested that self-similarity is maintained as long as the recording equipment has the frequency range to fully capture the radiated energy and Ide et al. [15] showed that careful accounting for path and site effects could increase the calculated stress drop for small events, bringing them into the self-similar range.

Continued improvements in laboratory earthquake sensing capabilities provide a further opportunity to investigate the self-similar scaling hypothesis. McLaskey and Glaser [16] demonstrated a high accuracy broadband sensor response using Glaser-type conical displacment sensors. They conducted Herzian impact study of ball drop calibration sources which were then used to characterize the AE sensors as having a 45 mV/nm sensitivity. They went on to apply the broadband, high precision sensing capability to study the micromechanics of asperity rupture on direct shear faults in both rock and Poly(methyl-methacrylate) (PMMA) which is used as an analog material free of the grain boundary scattering which significantly attenuates relevant frequencies in laboratory scale rock experiments [17]. The radiation patterns observed indicated that the laboratory scale rock fault asperity ruptures did not match the expected double couple source mechanism of an earthquake-like event, instead matching the expected pattern for asperity breakage rather than slip. In PMMA the contained rupture events—not reaching any free surface of the slider block—did behave according to the double couple source model. Finally, McLaskey et al. [18] reported full seismic moment tensors for laboratory events by a full-waveform comparison to forward model synthetic waveforms. This moment tensor catalog was included in the scaling results presented by Goodfellow et al. [11].

Selvadurai and Glaser [19] carried on with the use of Poly(methyl-methacrylate) as a rock-analog material, using its transparency to develop a further improvement in laboratory capabilities through the use of video recording for direct observation of the fault during slip. This technique is applied in Selvadurai and Glaser [20] to combine theoretical asperity interaction models rooted in contact mechanics with experimental results, diverting from the usual aggregate study of foreshock characteristics and interface strength to examine the strength of individual asperities. Here this work is continued and built upon by applying seismic inversion methods to study the source properties of laboratory earthquake-like events on the PMMA direct shear fault.

1.3 Seismic Inversion Methods

Source study in strong motion seismology quickly becomes a problem of inversion. A full moment tensor inversion (e.g. [21]) uses recorded waveforms and a model of wave propagation to characterize the energy of a source such that it can be represented as a combination of force couples. Improvements in sensor technology described above [22] allowed for the development of more rigorous, full-waveform study of laboratory foreshocks following the techniques used by strong-motion seismologists. Stable inversions of full moment tensors are computed at the laboratory scale with increasing frequency for experiments conducted in rock materials, which generally produce hundreds to thousands of events. Kwiatek et al. [23] used moment tensor and b-value results to study the evolution of fault damage in a granite sample. Confirming the McLaskey and Glaser [17] radiation pattern analysis, they observed relatively few double couple source mechanisms within the continuous flow of acoustic emission events. Stierle et al. [24] addressed the difficulties and sensitivities of moment inversions in laboratory rock experiments due to anisotropy in the rock material that changes according to the imposed stress. Their results also indicated that moment tensor inversions can be used to investigate anisotropic attenuation within a sample. In each case, laboratory moment tensor inversions were used in aggregate for the study of fault or material properties. An in-depth study of the source properties for individual laboratory events has likely not been considered because the laboratory scale rock experiments provide large catalogs suited to aggregate study and attenuate the very high frequency waves necessary for a finite source model.

Further information about the kinematics of an earthquake source can be inferred from a finite source inversion following Hartzell and Heaton [1]. This method inverts for the distribution and evolution of slip over a finite area during an earthquake source and has not been applied to laboratory earthquakes. As the quality of laboratory AE data and accuracy of system models continues to improve, particularly in PMMA as a homogeneous analog material, finite source inversion is reaching the verge of feasibility at the laboratory scale.

1.4 Summary of Goals

Understanding seismic sources both individually and as an aggregate phenomenon is a very active area of research. The contributions of laboratory experiments continue to grow in potential and recognition as experimental designs and methods are iteratively refined. Direct shear experiments in PMMA provide a unique opportunity to combine high fidelity acoustic emissions measurements and direct observation to measure and compare rupture source parameters including seismic moment, stress drop, and slip distribution. In the work presented, the development of a small catalog of 50 stick-slip events provides several opportunities to increase control, understanding, and precision within the experiment in pursuit of detailed source study. The question of scaling is addressed and the sensitivities limiting source inversion are investigated.

Chapter 2

Experimental System Setup and Characterization

This chapter describes the experimental apparatus, load and sensing components, system characterization, and sensor calibration. The core of the experiment is the direct shear fault between two blocks of poly(methyl-methacrylte) (PMMA). Under precise normal and shear loads, the fault produces bursts of elastodynamic waves, called acoustic emissions (AE), as millimeter-scale contact patches fail in the moments prior to full fault rupture. The AE events are monitored by an array of 16 conical displacement piezoelectric sensors which are absolutely calibrated. A pressure sensitive film was used between some experimental runs to provide a representative view of the typical distribution of real surface contacts.

Wave propagation through the plate is modeled by considering the complete seismic wave propagation in an elastic plate using a frequency-wavenumber formulation to compute Green's functions. A set of calibration events with known source properties are used to confirm the elastic properties used in calculation of the Green's function for the specific PMMA sample used in the experiments. The calibration sources are then used in combination with the tuned Green's functions to absolutely calibrate the piezoelectric displacement sensors.

2.1 Experimental Apparatus

Fault Configuration

The direct shear fault is oriented horizontally between a large PMMA base plate (612 x 612 x 38.5mm) and a narrow PMMA slider block (400 x 80 x 12.7mm), as shown in Figure 2.1. Below the base plate is a steel mounting plate for the piezoelectric displacement sensors. The PMMA base plate is supported by small cork patches distributed across the sensor mounting plate such that the bottom surface of the base plate can be approximated as a free surface. The base plate is fixed along the direction of fault motion by the reaction frame.

The slider block is approximately centered on the base plate and mounted vertically, such

that one 400mm x 12.7mm surface is in contact with the base plate to form the experimental fault. The load configuration is described in detail by Selvadurai [25]. The top of the slider block is press fit and glued into rigid aluminum loading platten. Two balanced hydraulic pistons apply normal force (F_n) on the fault and an electro-mechanical shear actuator coupled to the trailing end of the loading platten is driven at a constant velocity to increase shear force (F_s) on the fault.

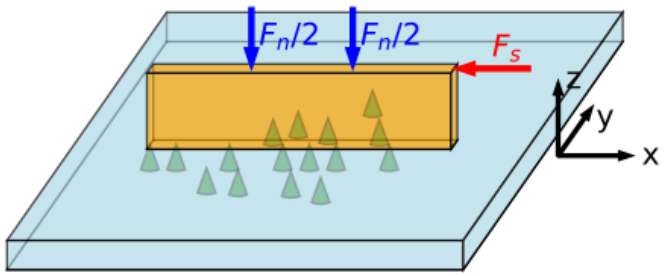

Figure 2.1: Schematic view of the experimental setup. The blocks are shown approximately to scale, with normal (F_n) and shear (F_s) loads where applied. The AE sensor array on the bottom of the base plate is at $z = 0$.

Instrumentation

Stresses on the fault are calculated from estimates of the loading forces. To calculate the normal force, the hydraulic pressure in the cylinders (P_h) is measured by a pressure transducer (OMEGADYNE PX329-2KG5V) and combined with the total area of the pistons (A_p). $F_n = P_h * A_p$ The shear force on the loading platten is measured directly by a load cell (OMEGADYNELC213-1K) mounted in the drive-train between the actuator and loading platten. The applied normal and shear forces are divided by the nominal fault area to calculate the stress state on the fault.

An array of 16 Glaser-type conical displacement piezoelectric sensors are mounted below the base plate in order to record acoustic emissions (AE) from slip events. These sensors have a broadband frequency response that is flat to within one order of magnitude from 10 kHz to 3 MHz and are absolutely calibrated as discussed later in this chapter. The AE

sensors have internal pre-amps, which are powered by up to 24 V on the line for maximum sensitivity. A digitizer (ELSYS TraNET EPC 16-bit dynamic range) is used to record AE signals at sampling rates up to 40 MHz.

A suite of 14 eddy current displacement sensors are mounted along the slider block, with 12 along the strike of the fault and 2 transverse to it. These sensors could help evaluate localized macroscopic slip along the fault but are not used in the current work presented.

Fault Surface

I attempted to make the fault surface as planar as possible. Efforts to machine the base plate revealed non-negligible internal stresses within the plate that warped the plate after every pass. The final plate has thickness varying from 38.3 mm to 39.2 mm over its entire 612mm x 612mm area. An average thickness of 38.5mm in the region of the fault is used in calculations. The error in Green's functions calculated assuming a constant plate thickness is expected to be small in general. Occasional outlying cases where the wave propagation is particularly sensitive to small errors in path length or reflection angle are treated as site-specific misfits.

The center strip of the base plate where the slider block is located was roughened by sandblasting. Although prior experiments succeeded with sandblasted surfaces on both the base plate and the slider block, I was unable to recreate an appropriate roughness profile by sandblasting the slider block. One particularly seismogenic fault was produced several years prior by commercial sandblasting but the setup and grit used were not documented. Attempts to prepare these fault surfaces by sandblasting with a setup available on campus made clear that this fault preparation method would require significant domain expertise to offer an appropriate degree of repeatability. My goal was to produce a fault surface roughness with well distributed millimeter-scale contact patches to provide a large enough rupture area for the imaging methods being developed. With the largest and most angular grit I found available for purchase (Black Beauty Abrasive Blasting Media 12-40 Mesh Size), the sand blasting was producing only tenth-millimeter-scale asperities.

In order to increase the roughness scale, experimental control and repeatability, an image of Gaussian noise was produced at the desired scale and laser engraved onto the slider block surface. The base plate was too large for the engraver and was left with the fine roughness of the sand blasting method. This was a novel technique which had several predicted possible failure mechanisms including insufficient laser precision to produce fine features within the millimeter-scale roughness, possible pixelation of the surface producing an unnatural and unstudied profile, and the possibility of melting rather than or in addition to ablation due to the laser pulses. No specific method was developed to address these issues beyond direct observation and application of the resulting surface. The final roughness profile used in experiments was developed simply by producing a handful of test patches that were evaluated by sight and feel. A FUJI pressure film was placed along the full fault interface and allowed to develop for ten minutes at high normal stress and zero shear stress. The pressure film results shown in Fig. 2.2 confirmed that a varied roughness profile with distributed, millimeter-

scale contact patches had successfully been imposed. Experimental loading of the new fault produced the desired seismicity, which is evaluated in detail in Chapter 4.

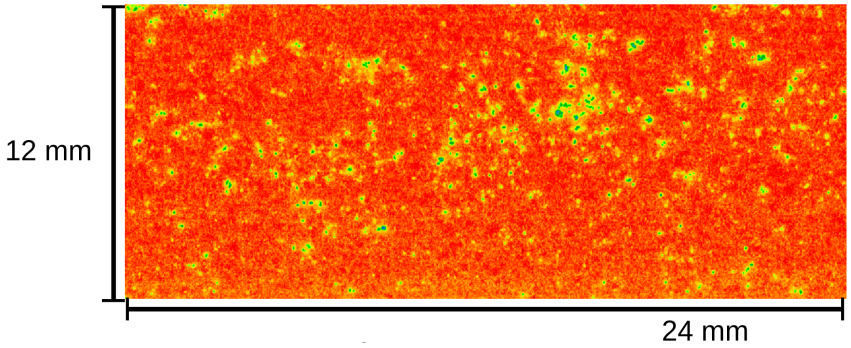

Figure 2.2: Sample section of FUJI pressure film taken from near the trailing edge of the fault interface. Fully red areas have negligible contact pressure and blue areas have the highest contact pressure. The lower block had a fine roughness from sandblasting and the upper block had laser-engraved millimeter-scale roughness dominating the contact area shown. A range of asperity diameters from approximately 0.1 mm to 1 mm is observed.

2.2 System Characterization

Calculating Green's Functions

Green's functions are the impulse response of the linear time-invariant system that describes wave propagation between two points on the plate, e.g. source and receiver locations. The Green's functions allow us to calculate a forward model of the expected displacements at sensor locations due to a known/assumed source input or to use recorded displacements to invert for source parameters. Since Green's functions are integral to the study of seismic and acoustic wave propagation, countless methods have been developed to calculate them for various Earth models and other systems. The homogeneous base plate is a relatively simple system so it is suited to more analytical methods of calculating Green's functions rather than heavily numerical approaches such as finite element modeling. Although the geometry of the plate with top and bottom free surfaces is rare in seismological models, it is possible to use a few existing and well-established programs. I evaluated programs based on two common analytical approaches: Generalized Ray Theory and Frequency-Wavenumber Integration.

A ray code was written in FORTRAN specifically for the case of a thick plate by Nelson Hsu at NBS in 1985 [26]. A Matlab translation of the code called PlateSoln, written by Greg McLaskey, has been used by the group in the past. The original code and translation produce vertical force-response Green's functions which were used to model calibration sources

Step	V_p $(mm/\mu s)$	V_s $(mm/\mu s)$	Q_p	Q_s	$f_{ref,p}$ (Hz)	$f_{ref,s}$ (Hz)	$CC_{80\mu s}$	$CC_{40\mu s}$	FAC
1	2.74	1.40	4000	1000	1.0E+07	1.0E+07	39	70	75
2	2.74	1.40	4000	100	1.0E+07	1.0E+07	56	82	79
3	2.74	1.40	200	100	1.0E+07	1.0E+07	53	80	81
4	2.74	1.40	4000	40	1.0E+07	1.0E+07	41	66	81
5	2.74	1.40	4000	20	1.0E+07	1.0E+07	12	15	80
6	2.74	1.40	4000	30	1.0E+07	1.0E+06	59	81	88
7	2.74	1.40	4000	25	1.0E+07	1.0E+05	43	68	88
8	2.74	1.30	4000	25	1.0E+07	1.0E+05	12	15	83
9	2.74	1.33	4000	25	1.0E+07	1.0E+04	62	82	88
10	2.74	1.33	4000	25	1.0E+07	1.0E+03	34	60	86

Table 2.1: Parameters evaluated during bracketing analysis for waveform modeling with CPS. The goodness of fit is measured by the cross-correlation (CC) coefficient for 80 μs and 40 μs after arrival, see Fig. 2.3a for example signal, and by the Fourier spectra amplitude coefficient (FAC). Step 9 was selected as the final model.

highly accurately to greater than 200 mm epicentral distances. However, when benchmarking the other single force responses against a fully analytical solution for direct arrivals I discovered that some responses and some ray arrivals are inverted in the results. The force couple responses critical to my analysis of earthquake-like sources are computed as spatial derivatives of the single force responses. While it may be possible to find and fix the errors in the ray code, it was more promising to try a different program instead.

Computer Programs in Seismology is a library of programs started by Dr. Robert Herrmann in 1981 with the goal of supporting rapid progress in seismic research [27]. The Frequency-Wavenumber Integration (FK) code included in the current suite supports models with both the top and bottom surfaces free. Although the laboratory scale plate is many orders of magnitude smaller than typical seismological modeling problems, the FK code is able to accurately model the plate in its true units so no careful scaling of the parameters or results is necessary. The FK code also includes the option of modeling frequency- and wave-type-dependent attenuation. Initial results modeling calibration sources with the same material properties as the ray code showed that the FK code is applicable but needed tuning to figure out the best fitting attenuation properties.

Tuning Material Velocities and Attenuation

Having confirmed that the code is able to accurately model the plate at my experimental scale, I used a bracketing analysis to identify the specific material properties that produced synthetic waveforms that best fit the calibration sources.

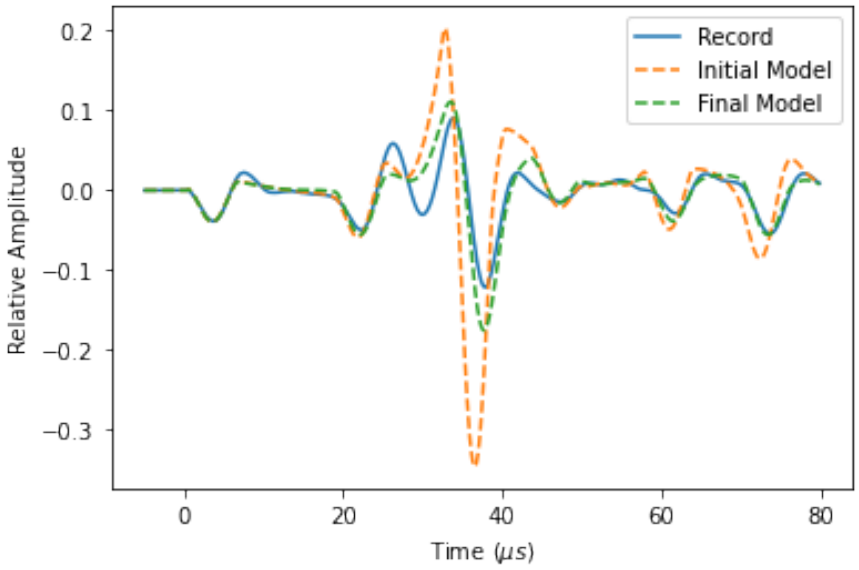

(a) Time Domain

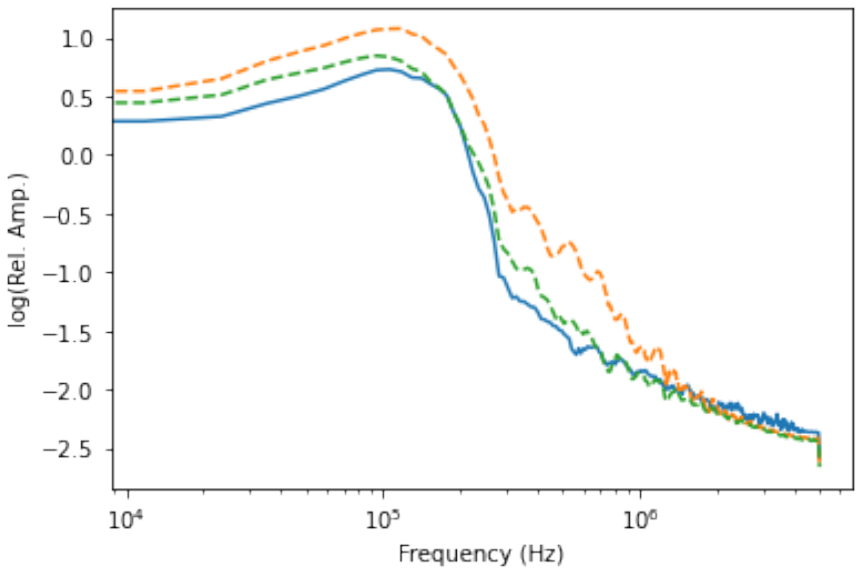

(b) Frequency Domain

Figure 2.3: (a) Example fits for station AE33. The initial model has a phase fit of 33 and amplitude fit of 86. The final model has a phase fit of 82 and an amplitude fit of 94. (b) The smoothed Fourier spectra of the record and models used to calculate the amplitude fit.

My initial estimates, final parameters, and several intermediate stages of the analysis are shown in Table 2.1. The table includes three goodness-of-fit measurements to characterize the improvements to the model: full waveform (80 μs) cross-correlation coefficient, early arrivals (40 μs) cross-correlation coefficient, and Fourier spectra amplitude coefficient, each out of a maximum score of 100. However, these metrics do not describe the systematic issues observed by visual inspection and addressed iteratively through the bracketing analysis. See Fig. 2.3 for two example fits, their Fourier spectra, and the corresponding fit metrics.

A constant plate thickness of 38.5 mm was used throughout the analysis. The compressional velocity of 2.74 $mm/\mu s$ was determined by the best-fitting least-squares source location results for a set of capillary fracture calibration tests with sharp onsets. The direct shear wave arrivals are generally too obscured by other arrivals to identify an arrival time and calculate the shear velocity. The initial shear velocity used in the model was an estimate based on prior work and modeling. By fitting a full waveform at each station rather than a single picked arrival time, the bracketing analysis provides an opportunity to determine a best-fitting combination of shear velocity and the interdependent attenuation parameters for shear wave quality factor (Q_s) and shear wave reference frequency ($f_{ref,s}$).

My initial shear velocity and attenuation parameter estimates (see example in Fig. 2.3) were close enough to synthesize a recognizable waveform and give information about how to proceed in tuning. Throughout this bracketing analysis, I used cross-correlation of the direct P arrivals to determine the scaling factor and any minor shift in timing ($< 1\mu s$) to improve alignment. The Green's functions units and calibration source force magnitudes are used to calibrate the sensors to absolute displacement units in the next section. The initial model has high quality factors and reference frequencies so that the effect of the attenuation not modeled by the previous Green's function code (PlateSoln) is minimal. These waveforms fit well at near distances and had increasingly poor fits to the magnitude and pulse shape of S arrivals at increasing epicentral distances. I progressively lowered the S quality factor in order to reduce the magnitude and increase the width of the S pulses at greater distances.

The value of Q_p varies widely with depth and temperature but is generally non-negligible (e.g. [28]). The modeled PMMA Q_p value is high enough at 4000 to have no significant effect on the pulse shape so I tried lowering it as well. The reduced P quality factor sufficiently reduced the magnitude of the direct P arrivals that the relative fit of later arrivals was made worse, particularly at large distances. The homogeneous PMMA used and modeled in these experiments is not a common earth material but rather a long-chain polymer. Kono [29] studied attenuation of shear and longitudinal waves in PMMA and found that in the relevant frequency and temperature range both wave types have similar exponentially increasing attenuation measured in dB/cm, with the shear attenuation values 3-5x larger than longitudinal. The quality factor Q is proportional to the change in amplitude $\Delta A/A$ per cycle [30] and the dB/cm values reported by Kono are proportional to $\log \Delta A/A$. Thus, the observed difference in Q_p and Q_s of at least three orders of magnitude is in line with expected material behavior.

I reduced the S quality factor to $Q_S = 20$, where I finally observed some stations with S wave arrivals modeled too low in amplitude. At $Q_S = 40$ all stations has S arrival amplitudes

too large so this gave me a narrow range to refine further. Within this range for Q_S, I noted that the late arriving pulses were still largely too short in duration and steep in onset. This indicated that I should increase the effect of Q_S at lower frequencies by reducing the reference frequency, $f_{ref,S}$. The ball drop signals used in the bracketing analysis have corner frequencies around 200 kHz (see Fig. 2.3b); capillary fractures and experimental sources around 1 MHz. My initial value of $f_{ref,S} = 10MHz$ was well above the frequency of my signals so it applied effectively constant attenuation. I reduced $f_{ref,S}$ to 1 MHz and confirmed that it did increase the apparent pulse duration of later arrivals, with a stronger effect for longer ray paths. At $f_{ref,S} = 10kHz$ and $Q_S = 25$ I found that all of the pulse shapes were close-fitting to my satisfaction but arriving too early.

I reduced the velocity v_s from 1.4 mm/μs to 1.3 mm/μs and found the arrivals too late, thus identifying another bracketed range. The final S velocity of 1.33 mm/μs, S quality factor of 25 and S reference frequency of 10 kHz (Tab. 2.1 step 9) produced visually and quantitatively satisfying fits. The reference frequency was not yet bracketed but one additional test with S reference frequency at 1 kHz significantly reduced the quality of the fit.

The quantitative fit metrics for the final (step 9) parameters are not significantly better than the intermediate results at $Q_S = 30$ and $f_{ref,S} = 1$ MHz (step 6). The synthetics for this model and are shown and compared to the final model in Fig. 2.4, demonstrating the minimal differences between the resulting synthetic waveforms despite several additional tuning steps. At this stage, further manual tuning has clearly diminishing returns on model improvement and a range of acceptable model parameter combinations has been identified. Based on the improvements to the model made in this brief, manual bracketing analysis, it is plausible that a systematic search through more of the parameter space could be used to find an even better fit. Although I was able to interpret effective model adjustments based on visual inspection of the waveforms, tuning one parameter at a time often improved the intended aspect of the fit while reducing others. Since the parameters are interdependent and the Green's function calculation is nonlinear a more thorough search would be resource intensive, whether in computation time for a broad search through the parameter space or experimental design time selecting an appropriate search algorithm and fit metrics. The development of such a search is beyond my current scope and questions of the potential improvement to experimental outcomes from both better system modeling and additional quantitative fit metrics are left for the discussion section. At some stage the marginal improvement from further honing the parameters is negligible compared to the other uncertainties due to physical imperfections (e.g. plate thickness, material defects) and signal processing limitations.

Absolute Calibration of AE Sensors

The AE sensors are calibrated to absolute displacement units by using the Green's functions to model two calibration sources with known or measured force functions following McLaskey and Glaser [16]: the ball drop and the glass capillary fracture. For ball drops, the force function is calculated by the formula provided by McLaskey and Glaser [16]. This force

Figure 2.4: Final (step 9) and intermediate (step 6) best fits from the bracketing analysis for all 16 stations. The recorded waveforms are plotted behind in red to show the remaining misfits. The intermediate model (blue) almost negligibly differs from the final model (black), despite the additional tuning steps. The model displacement amplitudes are labeled in nanometers and the recorded waveforms are scaled relative to the first arrival pulse. A 10 μsec timescale is included.

function has unquantified error based on momentum transfer to the plate, any initial velocity vector or minor height variation the ball has when manually released, and any imperfections in the impact of the ball on the plate due to e.g. a non-planar surface or dust particles. The capillary fractures were conducted with a load cell directly applying a gradually increasing force, leading to a step-like force upward when the capillary suddenly breaks and releases the normal load on the plate. The force function has error based on the low-frequency response of the load cell and its 15% measurement error. The resulting absolute force measurements have significant error from all of these factors but are still able to provide an absolute calibration to within an order of magnitude. By using the largest reasonable force estimate in both cases, a low estimate of the instrument sensitivity is produced. Displacement amplitudes and event magnitudes estimated using this calibration then represent the upper limits for those values.

As an initial confirmation of first-order agreement between sensors and across calibration sources, a simple cross-correlation is used to fit the arrival pulses. The synthesized waveforms are shifted by up to $+/-1\mu s$ based on the best-fitting lag from the cross-correlation to allow for unmodeled plate imperfections. The travel times vary from about 40 μs to 300 μs so the allowed shift could be up to 7% of the travel time but is generally 1-2% in practice. The observed sensitivities are all within an order of magnitude of 1 V/nm.

Many non-conical type laboratory acoustic emissions sensors and some types of seismometers have a significantly non-flat frequency response, requiring a filter-based calibration. We assume that the recorded waveform $r(t)$ is the linear combination of the source function $f(t)$ convolved with the Green's function $g(x,t;x',\tau)$ and the instrument/system response filter $i(t)$ so that $r(x,t) = f(x',\tau) * g(x,t;x',\tau) * i(t)$. If we combine the source-time function and Green's function as the synthesized ideal waveform $s(x,t) = f(x',\tau) * g(x,t;x',\tau)$, then frequency-domain division of the recorded and synthetic waveforms produces the frequency-domain system response from a calibration event $I(\omega) = R(x,\omega)/S(x,\omega)$. The frequency responses come out flat to within an order of magnitude, as expected for the conical displacement sensors based on prior calibrations by McLaskey and Glaser [22]. Using the frequency-domain system response requires a Fourier transform step even in analyses that otherwise take place entirely in the time domain. The observed frequency responses are sufficiently flat between 10 kHz and 3 MHz to forego this complication by using a simple scalar gain factor as previously calculated. Figure 2.5 shows synthetic waveforms converted to the original record units in Volts by the scalar gain factor in (a) and frequency-domain response in (b), demonstrating the effective equivalence in magnitude and added noise from transforms for the use of the spectral response.

2.3 Final Model Evaluation

The final model is the combination of estimated and tuned material parameters, assumptions supporting the calculation and use of Green's functions, and choice of instrument response function that have been outlined in this chapter. The quality of this model is integral to the

successful study of the experimental AE sources so I conducted a final round of testing with the calibration sources that uses the full model. The main experimental goals of this work focus on inverting recorded waveforms to solve for the source properties of stick slip events. Thus, an appropriate final test of the calibration data is to invert the recorded calibration event waveforms for the force source parameters and compare to the known inputs.

Force Source Inversion

The force sources used in calibration were represented as purely vertical forces that are exactly normal to the surface of the base plate. Multiple sources of error in the angle of impact are possible. For both the capillary fracture and ball drop sources it is possible that a perfectly vertical source would not be exactly normal to the plate surface since it was not possible to create a perfectly planar and constant thickness baseplate. The ball drops were conducted by manually releasing a 0.75 mm steel ball through a small hole in a membrane at the top of 4-cm-diameter tube 30.5 cm tall. Fortunately, the calculated impact force function is not very sensitive to millimeter-scale variations in drop height and initial velocity. Without considering any effect of air resistance on such a small ball, it would have an impact velocity greater than 2.4 m/s and dropping from 1 mm lower decreases the velocity by less than 2%. However, the ball drops could have small horizontal components that were not modeled but might be recoverable through inversion. For most of the ball drop calibrations, signals were recorded from the first four bounces. The angle of impact should increase for subsequent bounces as any initial small angle compounds and chances to interact with the confining walls of the drop tube increase.

The force inversion is set up by taking the equation for the displacment due to a three-component force source convolved with the plate Green's functions $u_z(x,t) = G_{jz}(x,t;x',\tau) * f_j(x',\tau)$ The source function components are assumed to have the same shape with only variation in amplitude such that $f_j(x',\tau) = a_j * f(x',\tau)$, where a_j are the component amplitudes and $f(x',\tau)$ is the source time function. The source time function is estimated from the recorded waveforms. Deconvolution of the source time function is theoretically possible but highly unstable. In this inversion, the source time function estimate is calculated separately and adjusted for best fit. The defined source time function is then convolved with the impulse response Green's functions so that $u_z(x,t) = [G_{jz}(x,t;x',\tau) * f(x',\tau)] * a_j$. The instrument response is also applied to the Green's functions in a forward sense rather than attempting another unstable deconvolution of the instrument response from the recorded waveforms. To solve for the force component amplitudes, the source time convolved Green's functions are inverted and applied to the displacements,

$$a_j = [G_{jz}(x,t;x',\tau) * f(x',\tau) * I(x)]^{-1} * u_z(x,t)$$

The records and Green's functions are filtered, windowed, and stacked for each station to form the right-hand-side matrices. A linear least squares inversion is performed with no weighting function applied.

Figure 2.5: Synthetics after force inversion for sample capillary fracture calibration event using (a) scalar calibration and (b) spectral instrument response. The spectral instrument response is applied to the synthetic waveforms by multiplication in the frequency domain rather than dividing it from the experimental records so amplitudes are shown in the recorded units of Volts. The spectral instrument response is not smoothed, resulting in the increased noise shown in (b). The result is shown for the removal of each individual station and little variation is seen, indicating stability in the inversion.

The stability of the inversion is tested by a jacknife approach of removing one or two stations at a time and comparing the results. Overall, the results are quite stable and most sensitive to the removal of the closest stations. Use of the spectral instrument response is also stable but the resulting synthetics have noise introduced from the un-smoothed frequency responses and domain transforms.

Capillary Fracture Inversions

The capillary fracture inversions indicate a force angle 13° - 15° off vertical, in the same direction for all three events. At first alarming, this result reveals an oversight in the capillary fracture experimental setup. This calibration force is applied by twisting a fine screw to lower a flat, 2mm-diameter tip onto the few-millimeter length of 0.1mm-diameter capillary tube. The screw is supported above the base plate by a long beam clamped at both ends so that no outside forces are applied in the region of the capillary break. The consistent angle of the applied capillary forces indicates that the loading beam was not mounted to be perfectly parallel to the plate surface.

The jacknife analysis shows the greatest sensitivity to the removal of stations nearest the capillary break, as shown in Fig. 2.5. Even those largest variations only result in a misfit first arrival amplitude at the most distant stations. The capillary force inversion is stable.

Ball Drop Inversions

The ball drop inversions are also stable. The most distant stations have relatively larger misfits but their removal makes little difference in the result. Each ball drop was recorded through four impacts. The ball loses energy as it bounces so that subsequent drops are expected to have decreasing force magnitudes. Later impacts also see any initially minor horizontal component of motion magnified by interactions with dust particles and the walls of the containing tube. The first drops have impact angles of 2° - 8°, with one outlier of around 20°. The subsequent bounces increase from the initially observed angle as expected.

2.4 Conclusions

The experimental system is equipped with precise, broadband displacement sensors which record acoustic emissions transmitted through the base plate. The AE sensors have a flat, broadband frequency response from 10 kHz to 3 MHz. Wave propagation from AE source to sensor through the base plate is modeled by Green's functions tuned to the PMMA material properties. The sensor calibration and Green's functions are combined to test the ability of a basic source inversion to return the calibration source properties. Both the glass capillary (step-like) sources and the ball drop (smooth pulse) sources are stably recovered by the inverse calculation. The system is now ready for detailed study of the source properties of contained acoustic emission events due to stick-slip motion.

Chapter 3

Early Imaging Efforts

Source study in strong motion seismology quickly becomes a problem of inversion. Stable inversions of full moment tensors, as described by Minson and Dreger [21] are computed at the laboratory scale with increasing frequency (e.g. ([23], [24], [11]). Further information about the kinematics of an earthquake source can be inferred from a finite source inversion following Hartzell and Heaton [1]. As the quality of laboratory AE data and accuracy of system models continues to improve, finite source inversion is reaching the verge of feasibility at the laboratory scale. In this work the demands and sensitivity of a finite source inversion algorithm adapted for the laboratory are investigated and it is then applied to state-of-the-art, absolutely calibrated acoustic emissions records from a PMMA shear fault.

The bulk of this chapter is taken from my submission to the 52nd US Rock Mechanics/Geomechanics Symposium in 2018. The experimental event catalog at the time was under-developed. I assumed that the several published successes in studying similar magnitude events as point sources would make a detailed point source analysis of newly recorded data superfluous rather than foundational. This work begins with forward modeling investigations using synthetic data based on event scaling estimates at the time which seemed to offer a proof of concept. However, attempts to apply the same method to the catalog of events produced effectively null results. Results from these early imaging efforts could not be confirmed or compared to simpler, trusted modeling of the events because the foundational point source analysis was also lacking. The work is included here as the proof of concept still stands. The failed application of the inversion method to recorded AE events motivated a step back to thorough documentation of basic event properties detailed in the next chapter.

3.1 Inversion Algorithms

Strong motion seismologists have developed a wide array of inversion algorithms with varying complexity, tailored to each application. The basic implementations of full moment tensor (point source) and finite source inversion are adapted for the laboratory. Use of single-component AE sensors simplifies the algorithms, although it also inherently provides less

information than three-component data.

Point Source Inversion

A full derivation of the forward problem can be found in e.g. To and Glaser [31]. Here the seismologic convention of moment tensor components combined with fundamental fault Green's functions as in Minson and Dreger [21] are followed such that the z-displacement due to a point source takes the form

$$\begin{aligned} u_z =& M_{xx}[\frac{\text{ZSS}}{2}\cos 2\phi - \frac{\text{ZDD}}{6} + \frac{\text{ZEP}}{3}] \\ &+ M_{yy}[-\frac{\text{ZSS}}{2}\cos 2\phi - \frac{\text{ZDD}}{6} + \frac{\text{ZEP}}{3}] \\ &+ M_{zz}[\frac{\text{ZDD}}{3} + \frac{\text{ZEP}}{3}] \\ &+ M_{xy}[\text{ZSS}\sin 2\phi] \\ &+ M_{xz}[\text{ZDS}\cos\phi] \\ &+ M_{yz}[\text{ZDS}\sin\phi] \end{aligned} \tag{3.1}$$

where ZSS, ZDD, ZDS, and ZEP are the z-displacement Green's functions for a vertical strike-slip fault, a 45° dip-slip fault, a vertical dip-slip fault, and an explosion, respectively. For fault slip constrained to the xy-plane with no opening or closing, only M_{xz} and M_{yz} can be non-zero. The other terms are left in the inversion as a check on physicality of the solution.

The 'beachball' focal mechanism diagram is used to plot point source moment tensors. An example focal mechanism for a perfect double-couple source on the experimental fault plane is shown in Fig. 3.1. Under ideal experimental conditions, the fault would slip in exactly the -x direction (rake of 180°). Since inversion results are rarely so perfect, the mechanism of the sample diagram has a rake of 165° to better illustrate the diagram orientations. Dark quadrants correspond to the tension axis with compressional first motions and light quadrants to the pressure axis with dilatational first motions [30].

Finite Source Inversion

A basic finite source inversion consists of discretizing the fault around the hypocenter into a grid of subfaults containing point sources and solving for the distribution of source energy across these subfaults. Hartzell and Heaton [1] outline a process for collecting all of the subfault contributions into one invertible matrix equation. The subfault synthetics are computed as template displacement records by convolving a simple moment rate function with each Green's function. A hypocenter is assumed and an appropriate delay is added to each synthetic to account for the rupture propagation time from the hypocenter. The inversion equation is set up as

$$Ax \cong b \tag{3.2}$$

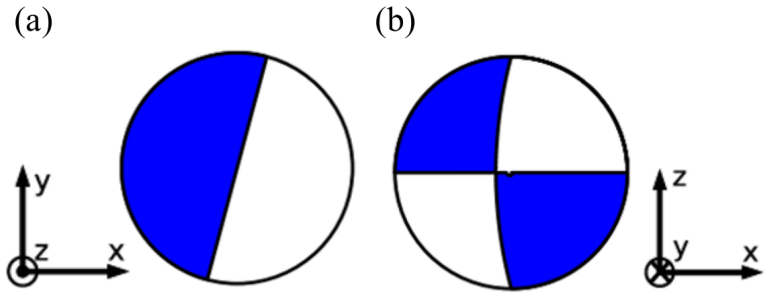

Figure 3.1: Beachball diagrams for a pure shear mechanism with slip in the xy-plane. The source has a rake of $\lambda = 165$ $\hat{u} \approx -0.96\hat{x} + 0.26\hat{y}$, $\hat{\nu} = \hat{z}$ to clarify the viewing angles of the diagrams. (a) Plan view of the slider block hemisphere of the beachball. (b) Front side view, as in Fig. 2.1, such that the fault is left-lateral due to the shear load. Plotted with ObsPy [32].

with A composed of the subfault synthetics and b containing the recorded displacement records such that x contains the magnitude of the moment contribution from each component of each subfault.

The inversion is massively under-constrained, thus there is no unique solution. Two of the additional constraints suggested by Hartzell and Heaton are applied: A moment minimization constraint pulls the solution toward the lowest total energy and a smoothing constraint applies a penalty to large source energy differences across neighboring subfaults. Finally, a non-negative least squares solution prevents negative interference between subfaults.

3.2 Synthetic Finite Source

Before attempting to invert recorded signals from un-characterized AE events, the quality and sensitivity of the algorithms are evaluated with synthesized event records. The point source inversion near perfectly inverts a synthetic point source, with decreasing accuracy for added noise.

Forward-Modeled Finite Sources

Two arbitrary finite sources are synthesized with mm-scale source radii as observed on the interface and by Selvadurai and Glaser [19]. The 'asperities' shown in Fig. 3.2 both have a pseudo-circular shape, constrained by the grid spacing, with radius $a = 0.4$ mm. One event, here named the center-source, has its hypocenter at the center. The other has its

hypocenter at the +x edge and will be called the tip-source. Rupture reaches each subsource at the rupture propagation velocity specified as $v_{rup} = 0.8v_s$. Each asperity has the maximum moment amplitude from its hypocenter and linearly decreasing amplitudes from more distant subsources. All source points have purely -x-direction slip contributions.

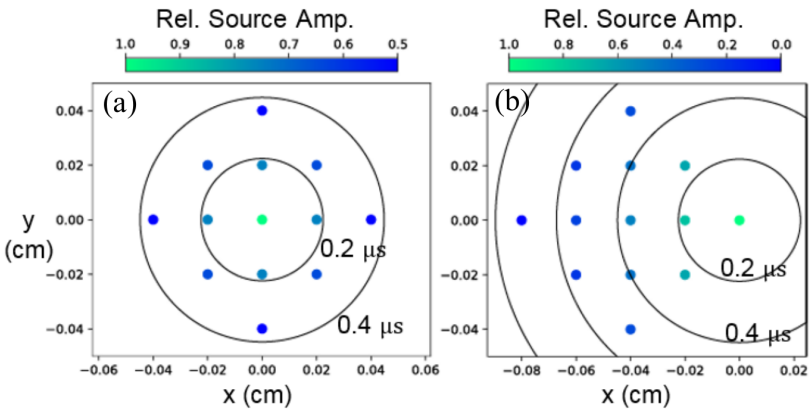

Figure 3.2: Source models used to compute synthetic event records. Each point source has a perfect $\hat{u} \approx -\hat{x}$ ($\lambda = 180°$) mechanism with amplitude indicated by the color bars and onset at v_{rup}/d from the hypocenter indicated by time contours. (a) A pseudo-circular asperity with hypocenter at its center. (b) The same asperity with hypocenter at the +x tip.

Point Source Inversion Results

First the point source assumption inversion results for the synthesized finite sources are examined. Both events had very similarly flawed solutions—only the results for the center-source are included for brevity. Three different filter pass bands were used for the inversions, revealing variation in the solutions. The records and solution fits are plotted in Fig. 3.3a for the widest pass band, with the upper corner at 1 MHz. A variance reduction (VR) metric is used to quantify the fit of the solution to the synthetic records

$$VR = (1 - \frac{\sum (d_{\text{rec}} - d_{\text{sol}})^2}{\sum d_{\text{rec}}^2}) \times 100 \tag{3.3}$$

(see Boyd et al. [33]). The VR ranges from 33.6% to 90.7% for stations within 10cm of the event origin. Of note within the records is that all of the first arrivals have the same sense, rather than the expected distribution of up-first and down-first motions from a double-couple source. Further investigation of this phenomenon is left to a future study since the test of the finite source inversion does not require a double-couple source.

The varied source mechanisms for three pass bands are shown in Fig. 3.3b. Although only x-direction slip was imposed on the synthetic asperities, the mechanisms contain a small

y-direction component at all frequencies. This initially implies that the spread of subsources beyond a single point obscures the information about slip direction, even if uniform across all the subsources.

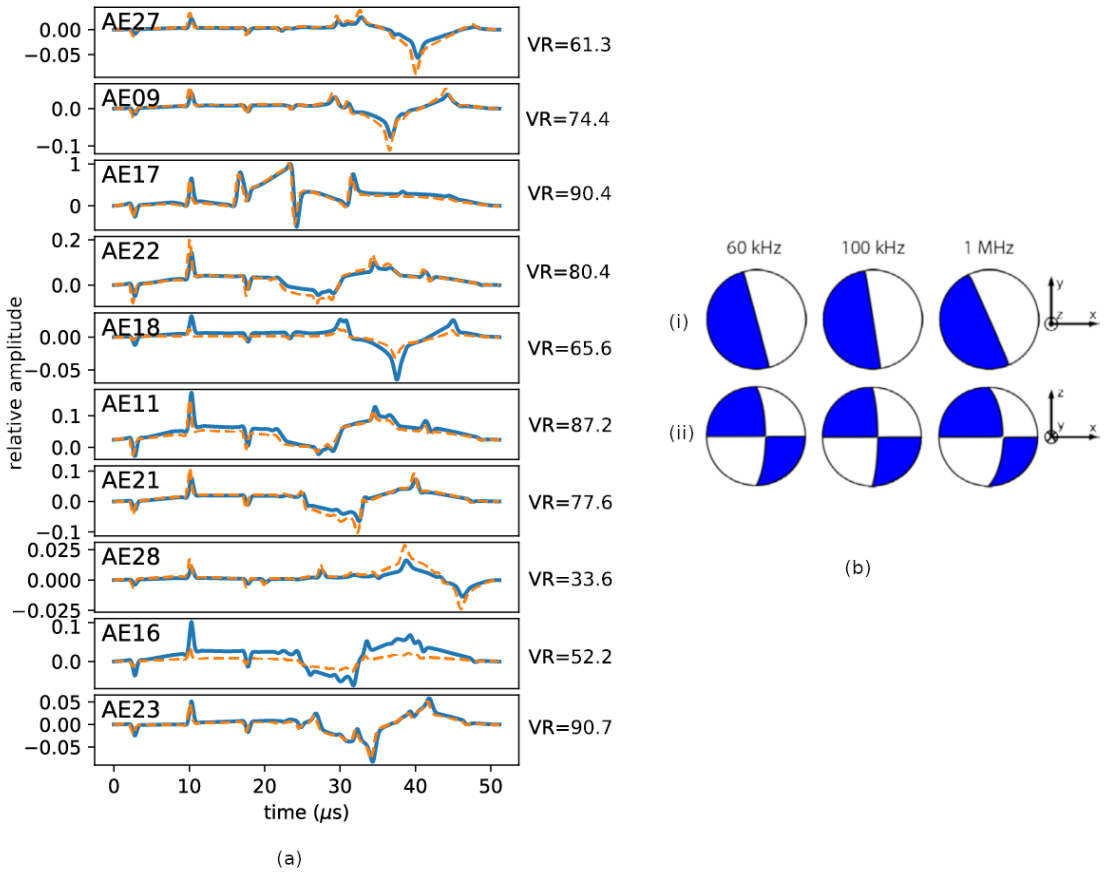

Figure 3.3: Results of the point source inversion for the simulated center-source asperity. (a) Synthesized records (blue) and point source inversion fits (orange, dashed) for the finite asperity with central hypocenter, at each station within 10 cm of the simulated source, shown for the highest-corner low-pass filter of 1 MHz. (b) Variation in point source mechanism with filter choice plotted as (i) plan views and (ii) front side views. Mechanisms plotted with ObsPy.

Finite Source Inversion Results

The first finite source inversions are approached slowly, with no imposed noise or any other sensitivity parameters added to the data or inversion. To further simplify, only negative x-

direction synthetics are used in the matrix. The resulting slip contributions for both sources are shown in Fig. 3.4.

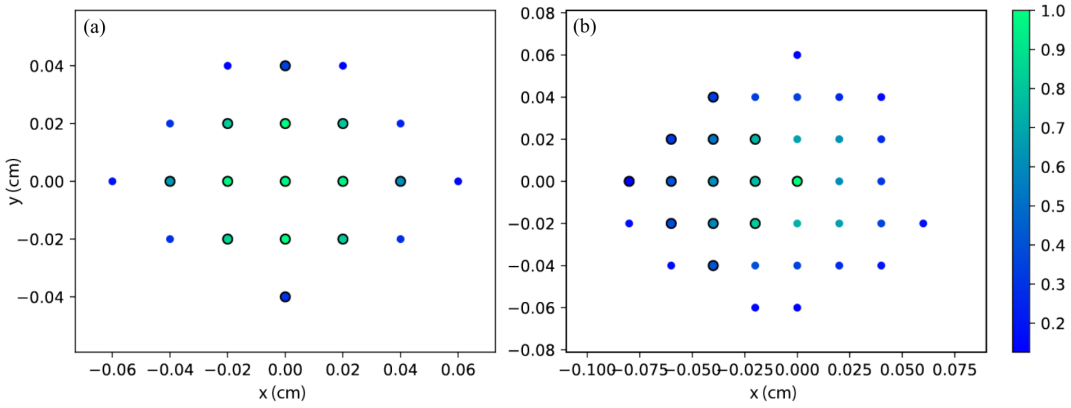

Figure 3.4: Finite source inversion results for (a) center-source asperity and (b) tip-source asperity. Dark circles indicate the point source locations of the forward-modeled events. Color indicates relative source amplitude, with the maximum source amplitude occurring at the hypocenter in both solutions.

Both sources correctly return the maximum source magnitude at the hypocenter and approximately correct amplitudes for all other points in the original source. Although the circle-source asperity is initially fully symmetrical, its inverse solution has an apparent bias toward sources spread in the x-direction. Despite the initial asymmetry of the tip-source asperity the result shows an inverse solution with strong symmetry around the hypocenter.

The tip-source solution also has a wider spread in the y- direction than the center-source. This spread is centered on the hypocenter at at the edge of the tip-source asperity rather than its center. Both of the original sources have linearly decreasing source amplitudes at the same rate. The amplitude decreases by half over one radius; so the sum of the amplitudes for the center-source is larger than for the tip-source and the tip-source hypocenter carries relatively more source weight than the center-source. Further study of additional sources with more comparable source weighting will be necessary to distinguish between sensitivities to sharpness in magnitude distribution versus asperity shape.

3.3 Experimental Inversion

With just the beginnings of an understanding of the abilities and limitations of this finite source inversion implementation, a preliminary inversion of recorded data is included here purely for demonstration of the expected application.

Sample Event Characteristics

A sample event is selected from a catalog of approximately 50 events detected from one direct-shear experiment with several stick-slip cycles. The event is one of 8 events that were large enough to trigger at least 12 of the 16 AE sensors deployed. Records from each of the sensors with a detectable P-wave arrival are shown in Fig. 3.5a stacked at their arrival times. First motions are distributed across the array with a clear radiation pattern indicating a double-couple mechanism with slip predominantly in the negative x-direction. The large amplitude and opposite sense arrivals at stations 22 and 27 locate the source near the middle of the slider block.

Point Source Inversion Results

Based on the observed radiation pattern, a point source mechanism similar to the example from Fig. 3.1 is expected. Instead, the result in Fig. 3.5b shows the computed mechanism with dominant slip in the positive y-direction, still in the fault plane. This apparent rotation is consistent across all pass bands used for the inversion. Since the raw data meets the expectations for slip in the x-direction, the rotation may be associated with the poor constraint on slip direction observed in point source inversion of the synthesized sources. However, this result combined with the previous findings leads us to suspect that a modeling error has entered into either the calculation or the azimuth-based combination of the Green's functions.[1] Error in the Green's functions or azimuths would not produce misfit in the fully synthetic trials because it would be present to the same degree in both the synthesized records and the solutions.

Preliminary Finite Source Inversion

Given the ambiguity in slip direction for this event, independent finite source solutions were computed for each of the negative x-direction and positive y-direction potential slips. Both solutions are plotted together in Fig. 3.5c. The relative source amplitude is plotted by color for the x-direction solution. The y-direction solution points are plotted without magnitude—their magnitude distribution has a similar mild degree of focus around the hypocenter as shown for the x-solution. All of the solution points are clustered in one quadrant of the full grid of subfaults. Unlike the synthetic source inversions, a symmetry about the hypocenter is not observed. From this very preliminary and low-confidence source solution, no conclusions about the observed source dynamics or comparison to any theoretical asperity slip models are appropriate to make yet.

[1] Author's note: the analysis of this chapter predates (and motivated) the renewed Green's function calibration and testing described in Chapter 2.

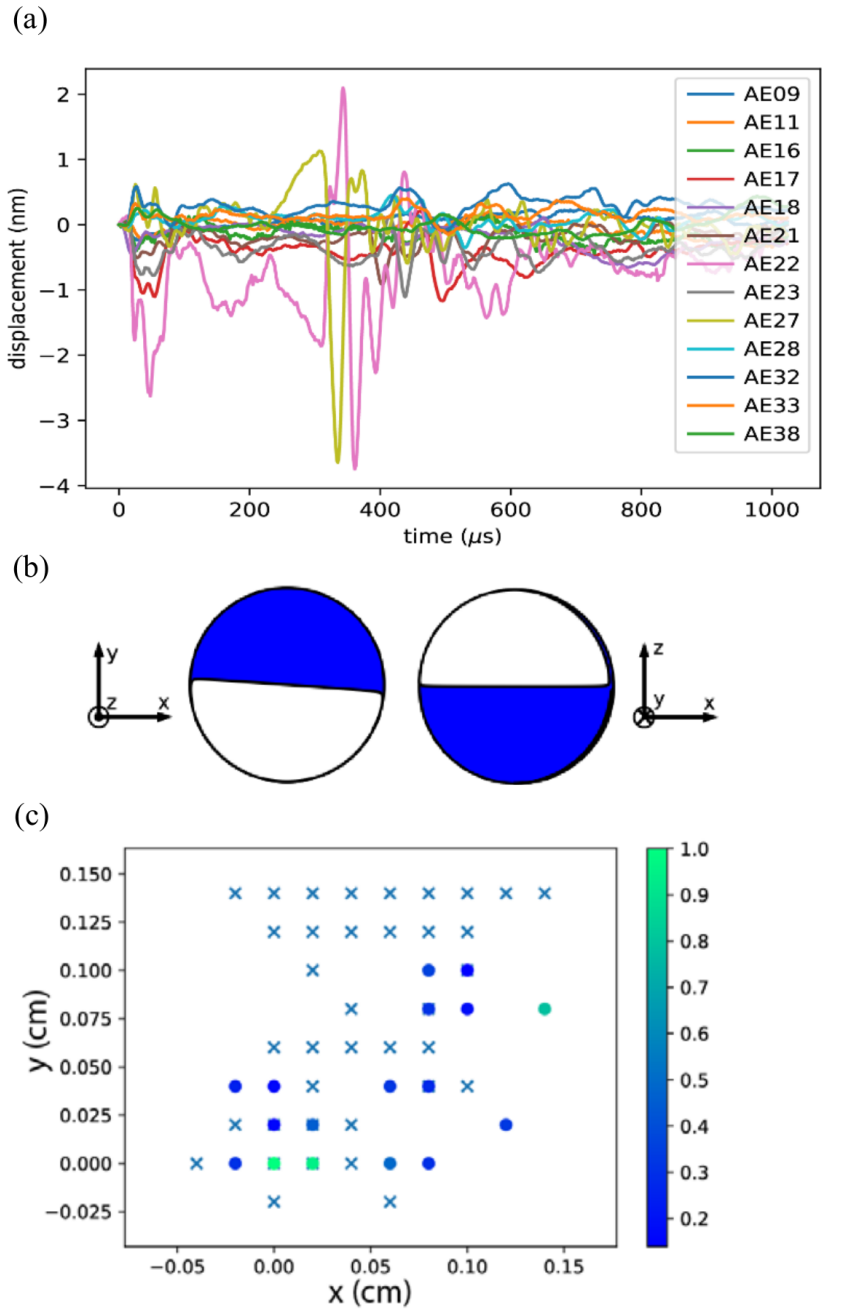

Figure 3.5: (a) Recorded waveforms for the example event, converted from raw voltage to displacement and stacked at their arrival times. (b) Plan- and side-view beachball diagrams showing the point source solution for the event, with dominant slip in the +y-direction. (c) Two preliminary finite source inversion results for the AE event with slip constrained to the x-direction shown as dots with magnitude information and slip constrained to the y-direction show as x marks.

3.4 Conclusions and Future Work

In this study, the earliest capabilities of a developing finite source inversion algorithm for laboratory applications are demonstrated. The simplest case shows that the inversion is possible but also quite ambitious. The first synthetic sources are highly arbitrary, a result of having limited grounds to predict what sensitivities would dominate in the inversion. Results from the first arbitrary sources have revealed probable sensitivities to magnitude distribution and hypocenter location, which will inform the next round of synthetic event designs. As understanding of the sensitivities of inversion in this environment grows the work will move toward adding complexity to the solution space. Allowing for unconstrained slip direction and more complex moment rate functions will allow the algorithm to more fully describe the kinematics of a complex AE source. Then as the complex inversion scheme's requirements for a trustworthy solution become clearer, it will become appropriate to return to the laboratory data for asperity rupture solutions that can be compared to the many proposed asperity slip models and contact mechanics descriptions.

Chapter 4

Developing the Laboratory Earthquake Catalog

Experimental events with earthquake-like source properties are expected to occur in the high shear stress moments prior to full fault rupture. This load condition is produced cyclically on the fault and AE data is monitored continuously. When a high amplitude, high frequency trigger is detected in the AE signal, a discrete block of time before and after the trigger is recorded on all 16 sensors. The blocks are scanned to detect full fault ruptures and possible contained AE events, which are then passed through a precise picking and locating algorithm. The dataset is incredibly rich with potential analyses—from further refining event detection methods to studies of magnitude scaling, frequency content, and source parameters. This chapter concludes with a brief investigation of potential magnitude scaling within the laboratory event catalog developed, which serves to further motivate the source studies efforts initiated in Chapter 3.

4.1 Experimental Process

The full experimental fault configuration and instrumentation is shown in Fig. 2.1. The direct shear experiment begins by increasing pressure in the hydraulic pistons to reach the desired normal stress on the fault surface. Next the shear actuator starts to increase shear stress on the fault surface by pushing the loading platten of the slider block at a constant velocity between .001 - .007 mm/s. The fault behavior shows a development phase for the first few minutes of shear loading during which several ruptures occurring at increasing failure stresses shift the fault to its strongest position. In the current experiment set, the first contained AE events are detected as precursors to the last rupture before the fault reaches its final, stable shear strength. The fault is then loaded continuously for tens of ruptures, cycling the shear stress in a sawtooth manner and producing from zero up to ten detected events per cycle. The slider block has a maximum travel of about 4 cm before the fault must be reset. The focus of this study is on testing the possibilities for detailed study of the

source properties of these individual events so additional investigation of the fault response to varied load conditions is beyond the current scope.

Acoustic emissions (AE) are monitored during all periods of increasing shear load by the array of vertically oriented piezoelectric conical displacement sensors mounted beneath the base plate (see Fig. 2.1). A software trigger records a block with 12.5 ms preceeding the trigger and at least 5 ms following it every time the signal slope exceeds 1 mV in 4 samples (0.1 μs). The majority of the recorded blocks are triggered by full fault ruptures. The contained AE events are generally clearly distinguishable from the background noise by their sudden onset broadband signals. The high frequencies stand out best from the noise, allowing an effective trigger setting, but many of the events detected are so small in amplitude that even a high-frequency-targeted trigger could not be tuned sensitively enough to catch them without causing frequent false triggers. This indicates that the recorded signals are unlikely to include every contained rupture that occurs during the experiment. A sample block which triggered on the full fault rupture and displays three precursor events is shown in Fig. 4.1.

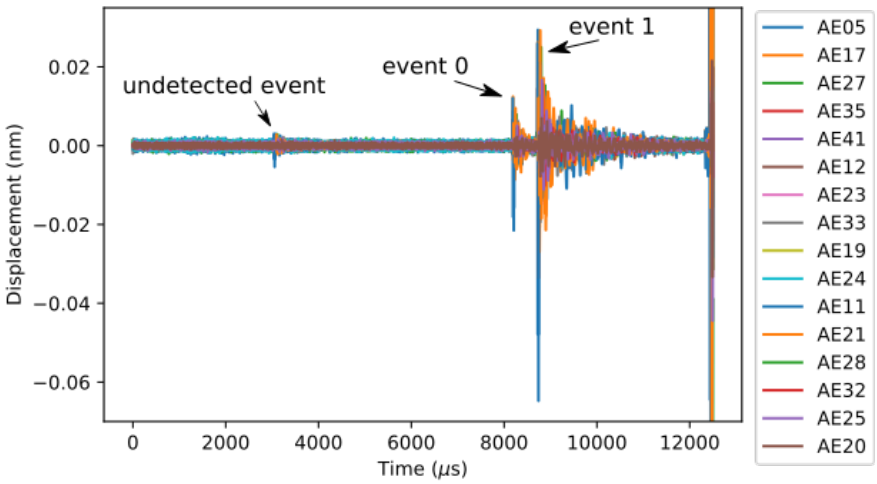

Figure 4.1: Demonstration of a trigger-captured block of AE signals from all 16 stations. The waveforms are filtered by a two-pole causal Butterworth filter to 10kHz-1MHz and converted from volts to nanometers displacement by a scalar gain factor (see Chapter 2). Three events of sudden onset, high frequency signals stand out from the background noise before the full fault rupture saturates all sensors.

4.2 Identifying Events

The experimental dataset presented here—the output of just one full sweep of the fault to its maximum displacement—includes 45 recorded blocks and at least 50 plausible asperity-scale rupture events. Attempts to manually find and pick all of the recorded events were both excessively time consuming and inconsistent, introducing unnecessary interpretative bias to the selection of individual AE events. The precise arrival time of each event on each station record is picked by a simplified Akaike Information Criterion (AIC) algorithm described below. The picking algorithm is effective on a limited signal window that includes an event arrival but it is not suited to scanning a long signal block to detect an unknown number of events. The raw voltage signals include relatively high amplitude and low frequency noise that obscures all but the largest AE events.

Exploratory filtering revealed that the 10 kHz to 1 MHz band shown in Fig. 4.1 removes the noise sufficiently to clearly reveal events with amplitudes varying by at least an order of magnitude. Event detection in seismic data is often done by a moving comparison of the short-term average and long-term average amplitude (STA/LTA, e.g. [34]). Prior to the exploratory filtering this method was completely ineffective in detecting all but the largest few events in the dataset. It likely could be applied after the filter removes the large-amplitude, low-frequency noise but would still require testing and tuning to select appropriate window lengths to detect the full range of events observed. Events could also be detected by careful application of an existing peak detection algorithm, such as the find_peaks method provided by the SciPy package [35]. Several early attempts at event detection for this dataset were oversensitive and resulted in much time lost to the development of additional logic sorting through possible events. For example, in order for a simple amplitude or even prominence-based peak detection to find the event labeled Event 0 in Fig. 4.1 it would also select at least one high-amplitude phase within the tail of Event 1.

The exploratory filtering results which show the events clearly within the 10 kHz to 1 MHz band also indicate that the highest amplitude noise is restricted to very high and very low frequencies. Rather than relying only on time domain observations, a spectrogram was used to investigate the variation of the frequency spectrum in the signal over time as shown in Fig. 4.2a. The events are not only still visible but also have significantly reduced tails at increasing frequencies. Although smaller amplitude events indicate smaller magnitudes which are associated with higher frequency components, the small amplitude and short signal duration appear to dominate such that small events have a decreased high frequency response within the spectrogram. The spectrogram is computed with the Scipy Signal module [35] and is most effective at revealing events in this dataset when calculating the power spectral density of the signal with moving windows of 512 points (12.8 μs) overlapping by the default 1/8th window. Taking the slice of the spectrogram just above 500 kHz intercepts all but the smallest visible events at a point in their spectra that provides a sharp peak which can now be detected by a peak finding algorithm as shown in 4.2b. The smallest event detected by this method has less than twice the amplitude of the undetected event shown in Fig. 4.2b. This approach was automated and used to scan the full dataset on one centrally-

located station (AE17), finding 50 frequency spikes around 500 kHz which are interpreted as plausible contained rupture events.

Picking Arrivals

With the spectrogram-identified set of probable event times, the simplified AIC algorithm for picking precise arrival times can be applied to a sufficiently short window on each station. The AIC originally splits a times series into two separate stationary intervals modeled by auto-regressive (AR) processes and finds the best-fitting order of the models in a least-squares sense [34]. Rather than determining appropriate AR coefficients for the noise and phase arrival on a seismogram, Maeda [36] simply used the variance of the signal on each interval. The first arrivals of a detectable event will have larger amplitude than the noise but generally maintain a zero-mean and thus the variance is increased for as long as the signal amplitude remains high. The simplified AIC formula for this approach is

$$\mathrm{AIC}(k) = k \log(\mathrm{var}(u[0:k])) + (N-k) \log(\mathrm{var}(u[k:N])) \tag{4.1}$$

and the phase arrival is taken as the minimum of the AIC. When the time series used ends while the signal amplitude is still large, the AIC has a consistent shape of a linear ramp down to the phase arrival followed by a steep step up to a flat region. High-quality AIC results with this character can be seen in the lower left corner plots of Fig. 4.3, where the narrowest pass bands are used on the highest amplitude signals shown. Low signal-to-noise ratio arrivals and too long time windows can disrupt the expected character, sometimes enough to shift the global minimum in the AIC away from the true phase arrival as seen in the right column of Fig. 4.3.

A secondary algorithm is applied to the AIC results to improve the quality of automatically determined arrival time picks. This step is designed to check for the sharp jump in the AIC indicating a true phase arrival. Yadav and Mishra [37] verify the global minimum by fitting a linear slope before and after, checking for a sufficient increase in slope after the pick. Plausible picks should be verified for the lowest amplitude signals possible, where the sharp slope in the AIC following the phase arrival can be brief and make it difficult to consistently fit a slope over an appropriate interval. Instead, the second derivative of the AIC function is taken and its peaks are detected, indicating the points of sharpest curvature. If the global AIC minimum detected is sufficiently close to a peak in the AIC second derivative then it is considered verified.

The two-step AIC arrival detection algorithm is demonstrated on four signals with decreasing amplitudes and filtered to four different bands in Fig. 4.3. The filtered displacement signal, simplified AIC function, and AIC second derivative are shown in each plot. Global minima are marked by circles which are filled if the pick was verified by a nearby second derivative peak, marked with x's. Appropriate filtering significantly decreases the noise amplitude relative to the signal, which increases the difference in variance detected by the AIC. At the broadest band—effectively the full broadband frequency content of the records—only

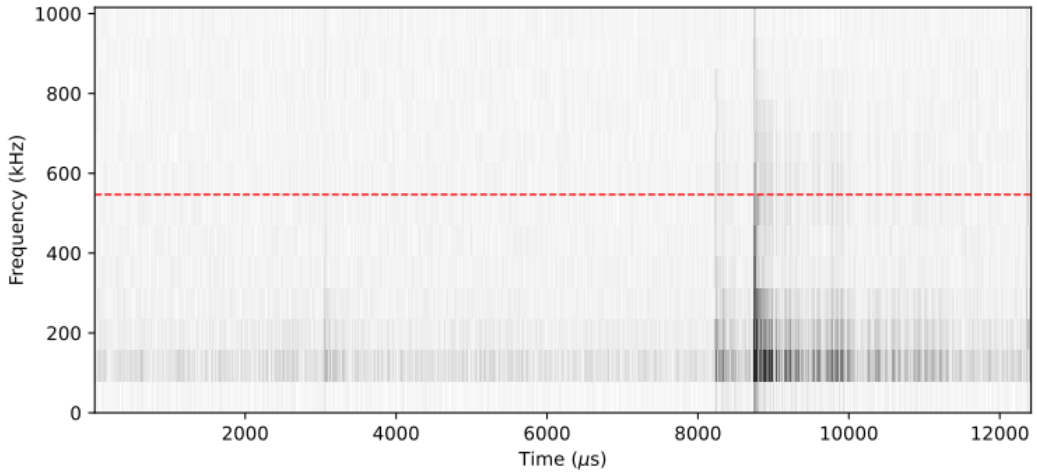

(a)

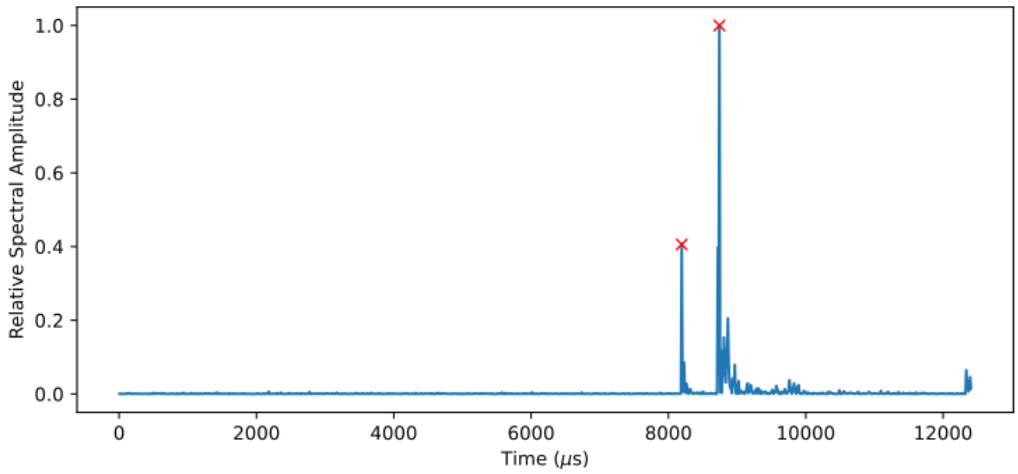

(b)

Figure 4.2: The spectrogram and single-frequency slice from station AE17 used for event detection. (a) Full spectrogram up to 1 MHz for station AE17 from the demo block shown in Fig. 4.1. The record is cut before the onset of the full fault rupture. The spectrogram results are raised the to .25 power before plotting to improve visual contrast. The red dashed line shows the slice plotted below. (b) Slice of the spectrogram for station AE17 taken at the red dashed line above. The spectrogram slice is normalized to its maximum value but not scaled by any power as was used above. Detected peaks are marked with red x's.

the highest amplitude arrival has a correctly timed global AIC minimum that is sharp enough to validate with a nearby second derivative peak. The AIC minimum on station AE19 appears near the event arrival but the noisiness of the signal has produced a sufficiently noisy AIC result that the minimum is too far before the sharp shift in the AIC for the pick to validate. As the frequency band is narrowed, the AIC results simplify and lower signal-to-noise ratio arrivals are able to be picked successfully. In the narrowest band, just 100 kHz to 1 MHz, the AIC results are most well behaved. On the noisiest signal, station AE25, the AIC gets sharpened near the first arrival as the pass band narrows but remains unable to pick it.

A causal filter is used in all picking applications so that no ringing is introduced prior to the arrival but a phase shift is applied. The phase shift results in a delay in the arrival which is larger for lower high-frequency limits. However, once the pass band is narrow enough to pick confidently the automated arrival time pick remains stable as the pass band is further narrowed. Since the AIC minimum will not occur until the second interval variance is different from the noise variance, the pick is delayed until the arriving pulse amplitude exceeds the noise amplitude. Filtered to lower frequency, the pick is delayed by phase shift; but filtered to higher frequency, the pick is delayed by larger noise amplitude. All of the automated picks are delayed by .05 - .5 μs from the apparent inflection point that would be selected as a manually picked arrival time. The signal onsets are sufficiently varied in amplitude, duration, and remaining noise trend that all attempts to consistently shift the automated pick back to the ideal manual pick failed. Fortunately, the delay appears generally consistent within an event such that source location calculations which only depend on relative arrival times (as described below) have higher confidence for the automated picks than for attempts at "improved" manual picks. In analyses that compare recorded displacement signals to Green's function models a cross-correlation is used to correct for this small timing error.

Event Locations

The picking results undergo a second form of validation when they are used to locate the AE event epicenters. An event location is calculated for each event by finding the least-squares solution to

$$t_{stn} = \sqrt{(x_e - x_{stn})^2 + (y_e - y_{stn})^2 + h^2}/v_p - c \tag{4.2}$$

where t_{stn} and (x_{stn}, y_{stn}) are the station arrival time and location, h is the plate thickness, c is the event origin time (before $t = 0$) and (x_e, y_e) is the epicentral location.

Even with the additional second derivative validation step in the automated AIC picker there are an unfortunately large number of false postive picks that result in failed locations. Attempting to locate each event with all of the automated picks, only 13 of the 50 events detected are successfully located. By using a jackknife approach to repeatedly remove one and then two stations from the picks before attempting the location calculation, some of the false picks are excluded and a total 22 events are successfully located. Some of the remaining 28 events could likely be located be the removal of additional picks, while others have arrival

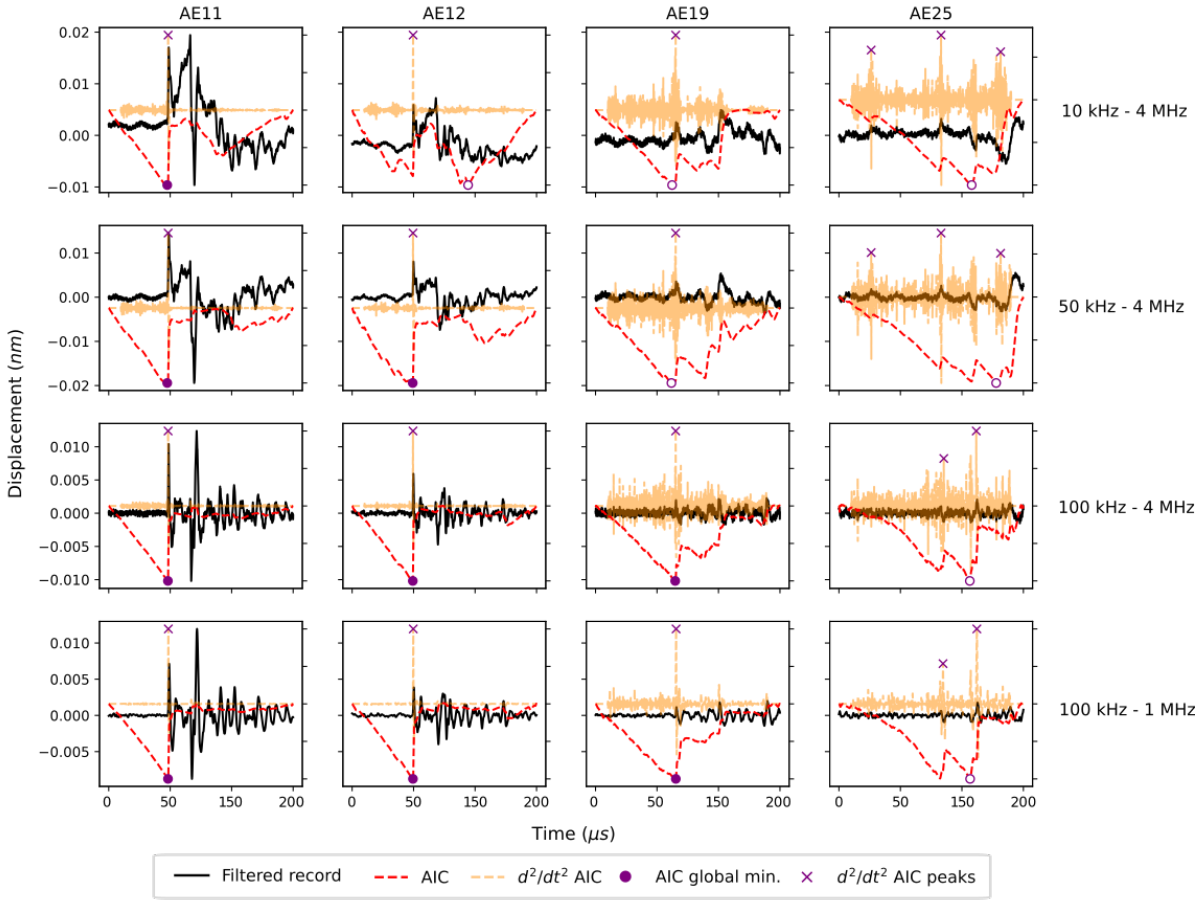

Figure 4.3: Demonstration of the two-step AIC picking algorithm used to automatically determine phase arrival times. Four stations are shown with decreasing amplitude and signal-to-noise ration from left to right. Four causal filter pass bands are shown with decreasing band width from top to bottom. The filtered displacement record is shown in black, zeroed and normalized AIC results are shown in dashed red, and the second derivative of the AIC is shown in orange. The global minimum of the AIC is marked by a purple circle which is filled if the pick verified against the second derivative. Peaks in the second derivative are detected with Scipy's find_peaks method in the signal package [35] and marked by purple x's.

times that are clearly inconsistent with a single event location—these events are left for later analysis.

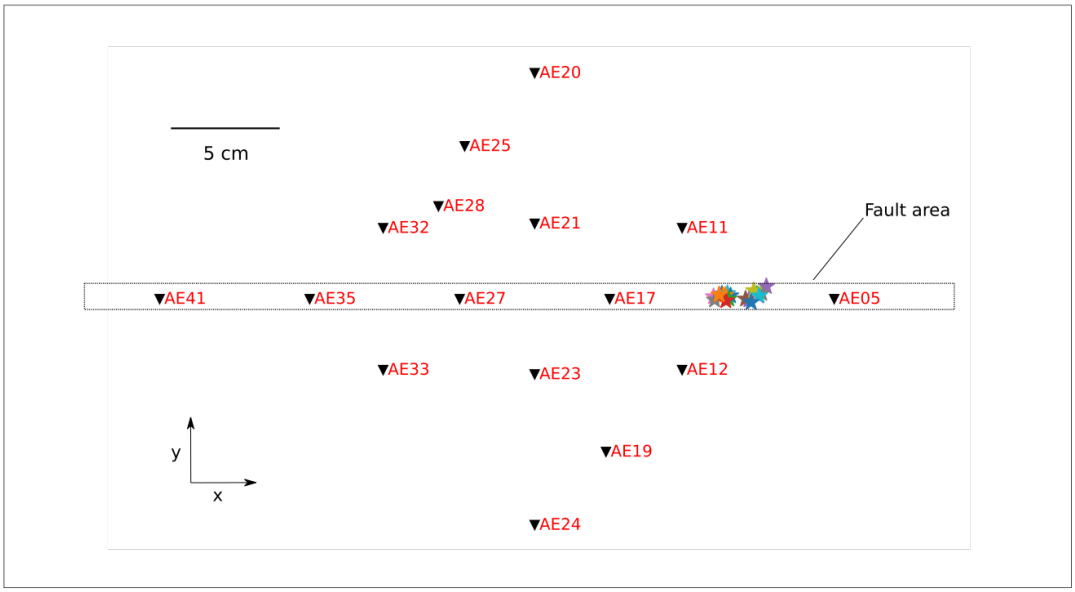

Figure 4.4: Plan view of event locations indicated by stars and sensor locations indicated by inverted triangles. All of the calculated event locations are clustered near the trailing edge of the slider block, which moves in the negative x-direction. The fault area is indicated by the dashed rectangle. The full extent of the 612x612mm base plate is not shown—the sensor array is approximately centered within it.

The locations of the 22 located events are shown on a plan view of the fault and station map in Fig. 4.4. All of the events are clustered within a small region of the fault near the trailing edge of the slider block. This provides a catalog of events which can be expected to have similar effects from any inhomogeneity in the plate or directivity in the sources, if present, since the azimuth and distance to each station is unchanging.

4.3 Investigating Scaling

The combination of broadband absolute displacement records and carefully tuned Green's functions is expected to provide enough experimental information for detailed source study. The magnitude and scaling of the AE events are estimated by two methods and results are compared. First an investigation of the source and scaling information transmitted by the first arrival (P-wave) pulse of the displacement records is conducted. A magnitude scaling

relationship is observed in the fitted pulse parameters, without using the Green's functions at all. Then an estimation of absolute seismic moment (magnitude) and rupture size is conducted by examining the amplitude spectra of the records and comparing to the forward model Green's function spectra. The magnitude and scaling results are presented in context with other laboratory and natural seismicity.

Fitting Arrival Pulses

A simple kinematic model for finite fault rupture is given by the Haskell source model [38]. The far-field (shortest ray path at least 10 times greater than source dimension) displacement due to a point source dislocation is proportional to the seismic moment rate of the source: $u(t) \propto \dot{M}_0(t - r/v_p)$. For a single point source with instantaneous (delta function) rupture, the displacement would follow a step function. Adding a finite "rise time" over which the moment accumulates at the point source by a linear ramp function, the displacement becomes a boxcar response. Finally, incorporating a finite fault area made up of a distributed set of point sources adds a rupture duration which is represented in the displacement response by the convolution of a second boxcar function. The complete displacement response to the Haskell source is then a trapezoidal function with a rise time matching the moment rate rise time and a duration representing the finite area of the fault [39].

The first arrival pulse for each station record of an AE event was automatically and independently fit with a two-parameter Haskell pulse. The arrival time for each record was determined either by the reviewed AIC pick or, for unpicked stations, the calculated arrival time based on the point source location. A 10 μs window around the arrival was filtered to 20 kHz - 1 MHz to simplify the pulse shapes and remove low frequencies acting as near-linear trends over the short window. For each rise and rupture time combination, a unit amplitude trapezoidal pulse was first cross-correlated with the filtered arrival pulse and allowed to shift by up to 1.25 μs to account for remaining error in the arrival times. The parameters for the best fitting pulse on each station were saved for each event. Since the pulse fitting was automated and a clear arrival pulse is not visible on every record, there is a large variance in the station-fit pulse parameters within each event.

The best fitting trapezoidal pulse length was also used to determine the extent of the arrival pulse on the filtered record, which was then integrated in time to calculate a station-specific parameter which is proportional to the seismic moment. As described above, the arrival pulse on a displacement record is proportional to the moment rate function of the source. Thus, the time integral of the pulse is proportional to the total seismic moment. This value is used to investigate self-similar scaling by plotting against the fitted rupture duration. Using a circular asperity model of radius a, the seismic moment $M_0 = \frac{16}{7}\Delta\sigma a^3$, where $\Delta\sigma$ is the static stress drop. The self-similar scaling behavior of seismic events shows constant stress drop, within four orders of magnitude, over at least twenty orders of magnitude of observed seismic moments [11]. The asperity radius is equal to the rupture propagation velocity, v_r, multiplied by the rupture time: $a = v_r * t_{dur}$. Eliminating the constants, self-similar scaling is indicated when $\int u_{arr}(t)dt \propto M_0 \propto t_{dur}^3$.

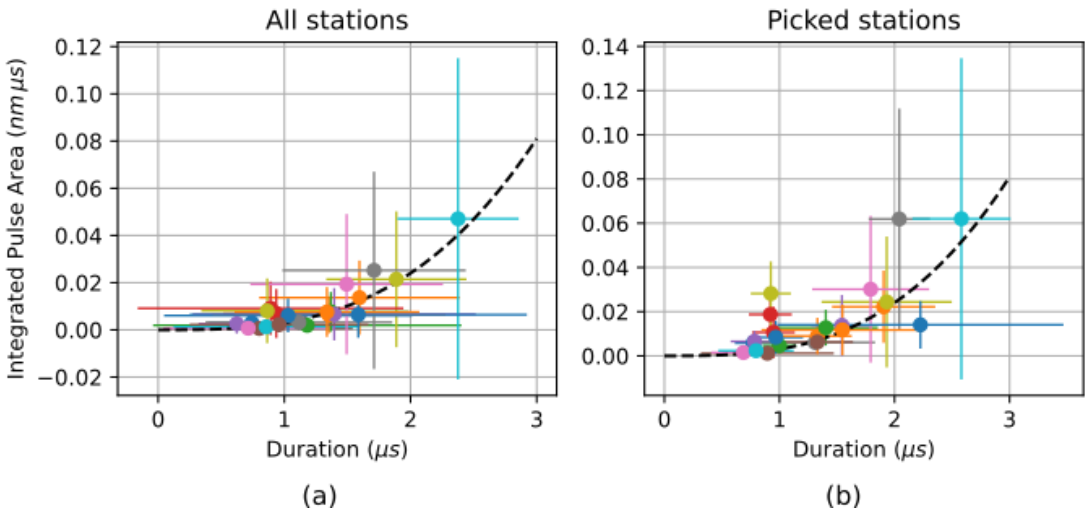

Figure 4.5: The integral of the first arrival pulse, proportional to seismic moment, is plotted against the average pulse duration for each event using (a) all stations and (b) only stations with picked arrivals. Each event is plotted in the same color on both plots. Error bars show one standard deviation for the area and duration calculated independently for each station within an event. A sample t^3 function is shown by the black dashed line; it is scaled by 3×10^{-3} in both plots.

Figure 4.5 shows the calculated pulse integrals plotted against best-fit rupture durations for all located events in the catalog. The large variances in duration and estimated magnitude-analog for each event are indicated by one-standard-deviation error bars. Removing the unpicked stations to focus the analysis on records with clearly detectable arrival pulses (as shown in Fig. 4.5b) does not significantly reduce the variance but does appear to introduce a slight bias toward higher magnitude estimates. A sample cubic trend is shown on both plots with a black dashed line. The results fit the cubic trend well, supporting the conclusion that this catalog of laboratory AE events follows the same self-similar scaling as observed seismicity at all other magnitude ranges [11].

Amplitude Spectrum Methods

In the frequency domain, the spectrum of the Haskell trapezoidal displacement pulse model is flat up to a first corner frequency representing the rupture duration and falls proportional to $1/f^2$ after the second corner frequency defined by the rise time. Often in practice the $1/f$ trend between the two corner frequencies is impractical to distinguish—due to rise and rupture times of similar magnitude and/or interference from secondary phase arrivals obscuring the low and middle frequency trends—so only one corner frequency is identified between flat and the $1/f^2$ trend.

The normalized displacement spectra for the events 0 and 1 which are detected, picked, and located for demonstration throughout this chapter are shown in Fig. 4.6. Trendlines for $1/f$ and $1/f^2$ are shown by the dashed and dotted black lines, respectively. For both events, the distinguishable corner frequency in the low 100kHz range is followed by an apparent $1/f$ trend, making it the first corner frequency representing the rupture duration for a finite area. Event 0 is smaller in amplitude and has a first corner frequency around 200-400 kHz, slightly higher than event 1 at 100-300 kHz. The second corner frequency for rise time is clearly above 1 MHz but obscured by noise in both cases. Although the sensors are calibrated with a flat gain up to the 3 MHz maximum frequency plotted, both events are small enough in amplitude that noise dominates the signal above 1-2 MHz. The corner frequencies were not directly estimated by this method for all events. Instead, the analysis and fitting of arrival pulses in the previous section was used to limit the range of assumed corner frequencies.

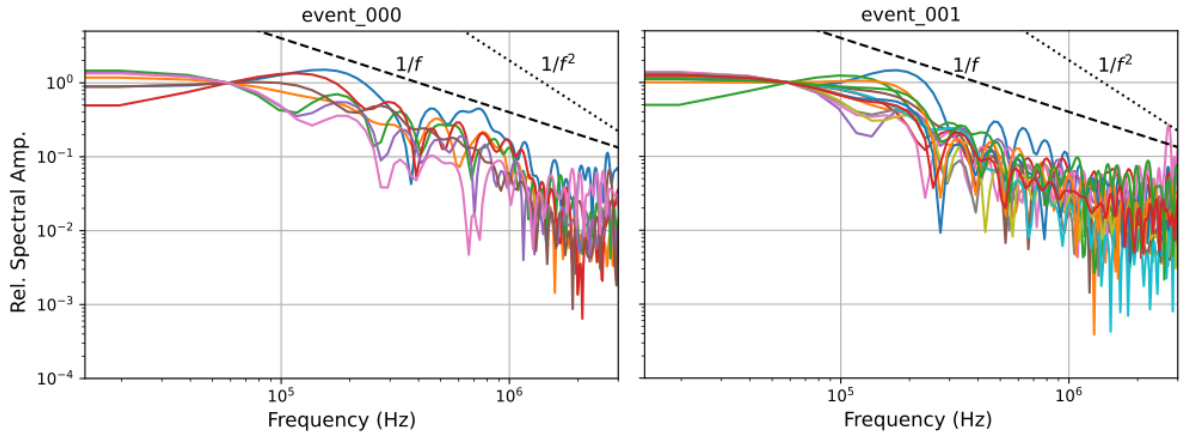

Figure 4.6: The normalized frequency spectra of the first arrivals for events 0 and 1 from stations with signal to noise ratios greater than 1.1 (calculated at frequencies below 100kHz). Sample slopes of $1/f$ and $1/f^2$ are shown by the black dashed and dotted lines in the upper right of each plot. Corner frequencies are estimated around 200-400kHz for event 0 and 100-300kHz for event 1.

The seismic moment measures the total moment released by a set of double couple sources covering the fault area. In the case of the point source model, the fault area is reduced to a an infinitely small point at the event hypocenter and the seismic moment is the magnitude of the moment tensor describing fault motion at that point [39]. Although the corner frequency investigation does indicate a detectable finite fault area, frequencies below the corner will have long enough wavelengths to sample the event as an effective point source. In this way, the seismic moment of an event can be estimated by measuring the spectral amplitude at low frequencies.

A seismic moment estimate is calculated from each station for each event by comparing the low frequency spectral amplitude of the recorded first arrivals to the that of the Green's function for a perfect, along-strike double couple mechanism at the point source location having unit seismic moment. Stations with less than a 1.1 signal-to-noise ratio at any point below 100 kHz are excluded and most remaining stations have signal-to-noise ratios ranging from 2-10. The AE producing region of the fault as seen in Fig. 4.4 has good azimuthal coverage in the -x half space which is the direction of slip for the slider block, and only one station in +x (AE05). The magnitude estimates from station AE05 are in range with the other estimates so no significant directivity is observed by this method. Most variation in the station magnitude estimates for each event is assumed to be a result of minor variation in the source orientation and station-specific site effects due to minor inhomogeneity not accounted for in the Green's functions modeling the plate. The results are shown as box-and-whisker plots for all located events in the catalog in Fig. 4.7. Each event has first and third quartiles within 0.5-0.75 magnitude units and many events have 1-3 outliers. The outliers are all from the most distant stations (e.g. AE41, AE35, AE33) which have both the lowest signal amplitudes and the largest expected error in the Green's functions. Thus, the median magnitude for each event is taken as the final magnitude estimate. The smallest event, event 30, has a estimated magnitude of Mw-7.5 and the largest, event 44, has Mw-6.4.

The seismic moment can also be estimated by the formula

$$M_0 = \mu A \bar{D} \tag{4.3}$$

where μ is the shear stiffness of the surrounding material, A is the rupture area, and $\bar{D}$ is the average slip over that area [39]. Using the simple circular asperity model [40], the rupture area can be estimated from a radius which is the distance the rupture can propagate during the estimated finite source time

$$A = \pi a^2 = \pi (v_{rup} t_{dur})^2 \tag{4.4}$$

The rupture velocity is estimated as $v_{rup} \approx 0.8 - 0.9 v_s$ [30]. The slip $\bar{D}$ can also be estimated by combining a slip velocity with the estimated rise time, t_r, which represents the duration of slip for each particle on the fault surface. Typical slip velocities seismicity in rock materials are on the order of 100 cm/s [39]. Lay and Wallace [39] show a simple stress and strain analysis starting from Brune's model of fault slip which provides an explicit calculation for the slip velocity based on stress drop such that

$$v_{slip} = \Delta\sigma (v_s / \mu) \tag{4.5}$$

However, rather than assuming either a typical slip velocity or stress drop based on seismicity at other scales or in other materials, this analysis can be rearranged to use the estimated rupture area and spectral moment estimate to compare the static stress drop to other reported seismicity. Figure 4.8a shows the event magnitudes plotted against the estimated circular source radius calculated using $v_{rup} = 0.9 v_s$. Constant stress drop lines calculated by

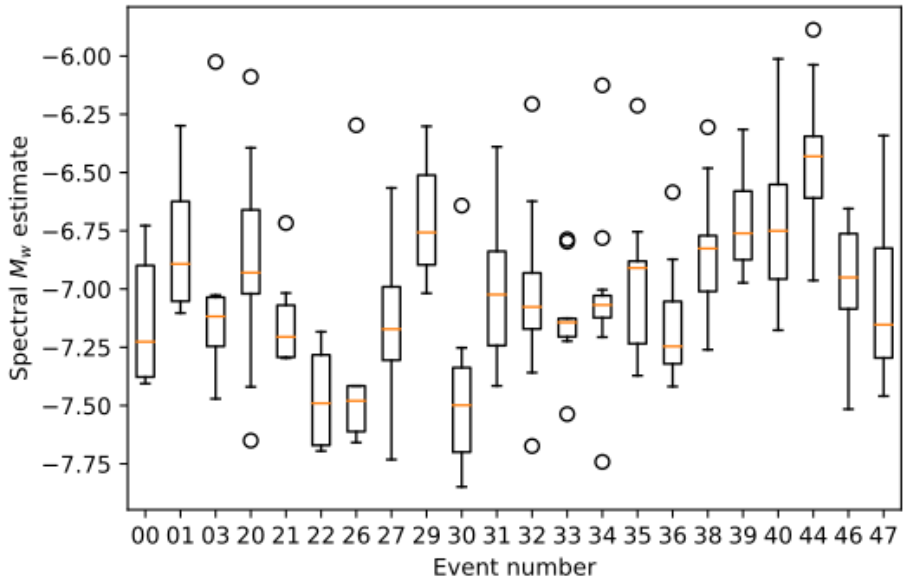

Figure 4.7: Moment magnitude estimates for all located events in the catalog shown as box-and-whisker plots. The whiskers show the first and third quartiles of the magnitude estimates calculated at each station. The median value marked by the orange line in each box plot is taken as the estimated event magnitude.

$\Delta\sigma = (7/16)M_0/a^3$ for a circular asperity are shown for typical values from 0.1 - 100 MPa. As expected based on the initial scaling analysis shown in Fig. 4.5, the absolute magnitude and duration estimates indicate stress drops which are narrowly grouped over one order of magnitude in stress drop. Figure 4.8b is a summary plot taken from Goodfellow et al. [11] to demonstrate how the estimated event sizes fit into the greater context of natural and laboratory seismicity. Not only are the events grouped following the self-similar scaling of constant stress drop, they also fall within the same range of stress drops observed in seismicity at all scales. Using the paired equivalent axes on this figure, it can also be seen that the approximate source radii of 1-3mm appropriately match the observed corner frequencies in the low 100s of kHz. The slip velocity implied by a stress drop of 1 MPa for the PMMA material properties is approximately 500 cm/s. This is higher than the typical value in rock materials because the density is lower, resulting in a higher v_s/μ ratio and lower inertia.

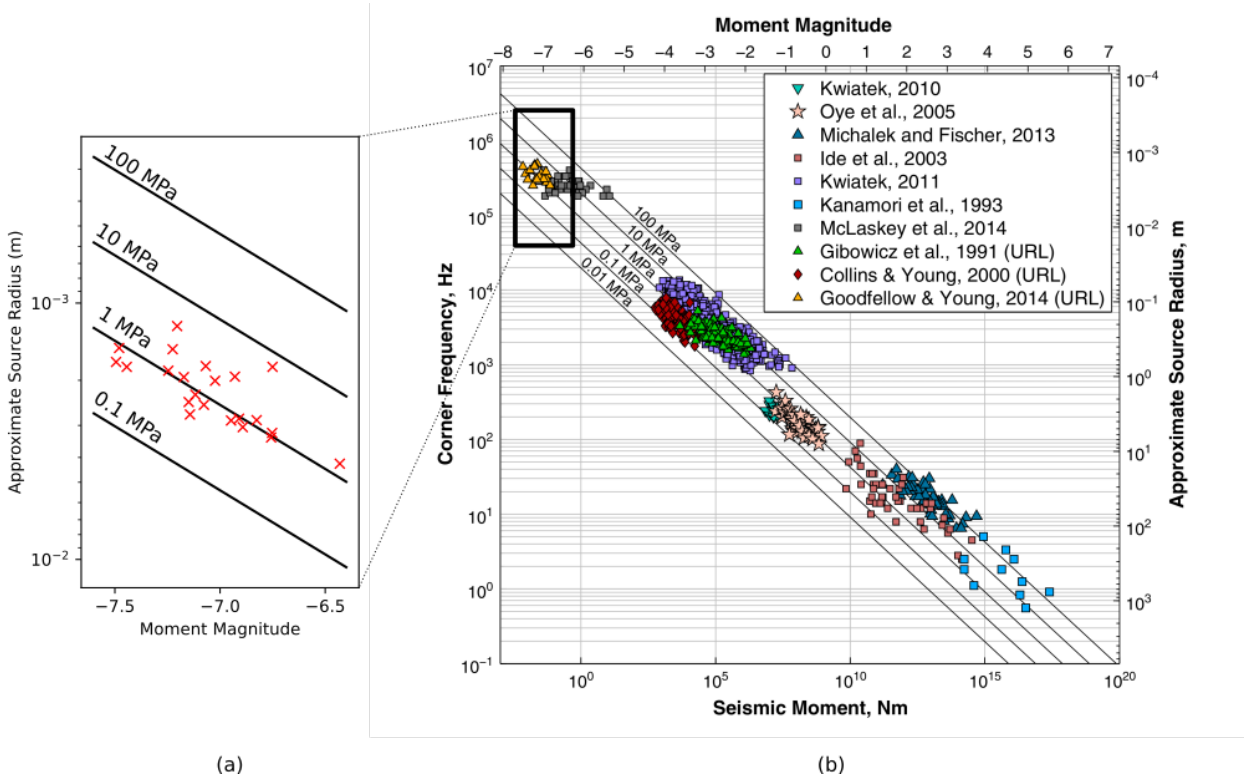

Figure 4.8: The relationship between estimated seismic moment magnitude, asperity radius, and stress drop shown in context with natural seismicity as well as other laboratory seismicity. (a) The spectrally estimated event magnitudes are used to calculate a moment magnitude and the trapezoidal pulse source durations are used to calculate the source radius, with $v_{rup} = 0.9v_s$. (b) Summary figure as published in Goodfellow et al. [11]. The boxed area shows the bounds of the plot in (a). The stress drop lines on both plots are calculated for a circular asperity described by Madariaga [40] such that $\Delta\sigma = (7/16)M_0/a^3$ [39].

4.4 Catalog Results and Discussion

Of the 50 AE events detected in the experimental dataset, 22 were successfully picked and located through an automated process. These 22 events have estimated moment magnitudes ranging from Mw-7.5 to Mw-6.4, approximate source radii of 1-3mm, and stress drop on the order of 1 MPa. The seismicity follows the self similar scaling that results in a narrow range of stress drop values over twenty orders of magnitude variation in seismic moments and faults in a variety of rock and rock-analog materials.

The source radius estimates of 1-3mm are near the asperity scale observed by the pressure film imaging of the fault surface in Chapter 2 and nearly an order of magnitude larger than the synthetic asperities used in the early finite source study of Chapter 3. At the largest

estimate, one would expect to see an asperity with contact area equal to a 6mm diameter circle. No individual asperities that large were observed; however, some regions of densely spaced asperities of 1 mm diameter each and a total diameter of several millimeters are present. The largest events observed may be the result of rupture over a multiple-asperity patch. In the broadband records, complex arrival pulses such as those shown in Fig. 3.5a are often observed and further support the possibility of a complex rupture. The initial finite source efforts targeting the observed single asperity scale are likely misguided—allowing for a larger anticipated rupture area will likely lead to a more manageable inversion scale and a more revealing picture the contained rupture events.

Chapter 5

Conclusions and Future Work

5.1 Conclusions

This work was undertaken with the goal of using high fidelity observations collected from a direct shear experiment in PMMA to conduct a detailed source study and finite inversion. The experimental setup and sensing capabilities were first characterized and confirmed to have the precision necessary to support source inversion at the scale of millimeter asperity rupture. An attempt to move ahead with developing the finite source inversion method for the laboratory was initiated with an investigation of the forward model results. These forward models behaved approximately as expected in the simplified point source analysis and the finite inversion. However, it was not possible to verify the method on an experimental event record because it did not behave as expected, in either the finite inversion or the simpler point source inversion. This failure motivated a return to a more thorough catalog development and basic seismic analysis, recognizing that the increasing reports of successful point source inversion of laboratory AE events does not make the process entirely straightforward. The investigation of magnitude scaling within the observed catalog revealed that the event records indicate a slip dimension (1-3 mm radius) larger than the size of any individual asperity on the roughened fault surface (up to 1mm diameter).

The analysis provided opportunities for the development of new and improved experimental techniques. When the surface preparation by sand blasting was found to be difficult and inconsistent, it was replaced successfully by highly controllable laser engraving. This new approach was quick to implement and test, with just a few rounds of adjusting engraving parameters by feel resulting in a surface that produced the desired level and scale of seismicity. The spectrogram-based event detection approach developed appears to be a new approach within the field. Automatic event detection and picking was not intended to be a main focus of this work but it is an active field due to the demonstrated difficulty in pick consistency and quality (e.g. Ross et al. [41], Peidong et al. [42]). The AIC picking process was also extended by the use of the second derivative to find sharp bends in the simplified AIC function which are more likely to indicate true phase arrivals. The methods and code

developed are available on github.

5.2 Future Work

The detailed study of the laboratory event source properties presented here did not reach the point of full finite source inversion as intended. The catalog and scaling analysis required substantial refining work and the development of new techniques as described above. However, the results of this analysis support and motivate the continuation of this work. The apparent mismatch between event magnitude and the maximum single asperity dimension on the fault further motivates the detailed source study efforts by indicating that the events observed in this data set may have complex slip occurring over multiple nearby asperities. Work with the existing experimental data could continue where this analysis leaves off—with a careful study of the point source inversion results and sensitivities followed by further development and application of the finite source inversion method.

The laser engraving surface preparation demonstrated provides ample opportunity for experiments testing existing hypotheses about the effects of various surface roughness models on stick-slip fault motion. Candela and Brodsky [43] observe a transitional scale where grooving is no longer observed on faulted surfaces. Grooves are created when a high strength asperity slides over a lower strength surface. They show that the aspect ratio (average asperity height divided by profile length) increases at the very small scale where grooves stop appearing and propose that above a specific aspect ratio asperities begin to yield plastically. Laser engraving could be used to impose surface roughnesses with a range of aspect ratios to directly study the resulting asperity slip mechanisms using source inversion results or radiation patterns as in McLaskey and Glaser [17]. Brodsky et al. [44] scanned natural fault surfaces from the millimeter to meter scale using laser profilometry and lidar, which could allow for an existing fault surface to be reproduced directly on a PMMA surface. The fully-implemented combination of controlled fault roughness, detailed source and slip inversion, and potential direct observation of the slipping surface would provide an enormously rich potential for laboratory study of earthquake-like sources and sliding friction more generally.

Bibliography

[1] S. H. Hartzell and T. H. Heaton, "Inversion of strong ground motion and teleseismic waveform data for the fault rupture history of the 1979 Imperial Valley, California, earthquake," *Bulletin of the Seismological Society of America*, vol. 73, no. 6A, pp. 1553–1583, Dec. 1983, ISSN: 0037-1106. DOI: 10.1785/BSSA07306A1553. eprint: https://pubs.geoscienceworld.org/ssa/bssa/article-pdf/73/6A/1553/5331847/bssa07306a1553.pdf. [Online]. Available: https://doi.org/10.1785/BSSA07306A1553.

[2] W. F. Brace and J. D. Byerlee, "Stick-slip as a mechanism for earthquakes," *Science*, vol. 153, pp. 990–992, 3739 1966. DOI: 10.1126/science.153.3739.990.

[3] H. F. Reid, *The elastic-rebound theory of earthquakes*, eng, ser. University of California, Berkeley University of California publications on geological sciences ; v. 6, no. 19. Berkeley, CA: University of California Press, 1911.

[4] J. H. Dieterich, "Modeling of rock friction," *Pure and Applied Geophysics*, vol. 84, pp. 2161–2168, B5 1979, ISSN: 0033-4553. DOI: 10.1007/BF00876539.

[5] J. R. Rice and A. L. Ruina, "Stability of steady frictional slipping," *Journal of Applied Mechanics*, vol. 50, p. 343, 2 1983, ISSN: 00218936. DOI: 10.1115/1.3167042. [Online]. Available: http://appliedmechanics.asmedigitalcollection.asme.org/article.aspx?articleid=1406945.

[6] T. Baumberger and C. Caroli, "Solid friction from stick-slip down to pinning and aging," *Advances in Physics*, vol. 55, pp. 279–348, 3-4 2006, ISSN: 00018732. DOI: 10.1080/00018730600732186.

[7] D. Lockner, "The role of acoustic emission in the study of rock fracture," *International Journal of Rock Mechanics and Mining Sciences & Geomechanics Abstracts*, vol. 30, no. 7, pp. 883–899, 1993, ISSN: 0148-9062. DOI: https://doi.org/10.1016/0148-9062(93)90041-B. [Online]. Available: https://www.sciencedirect.com/science/article/pii/014890629390041B.

[8] H. Kanamori and D. L. Anderson, "Theoretical basis of some empirical relations in seismology," eng, *Bulletin of the Seismological Society of America*, vol. 65, no. 5, pp. 1073–1095, 1975, ISSN: 0037-1106. DOI: https://doi.org/10.1785/BSSA0650051073.

[9] K. Mayeda and W. R. Walter, "Moment, energy, stress drop, and source spectra of western united states earthquakes from regional coda envelopes," eng, *Journal of Geophysical Research: Solid Earth*, vol. 101, no. B5, pp. 11 195–11 208, 1996, ISSN: 0148-0227. DOI: 10.1029/96JB00112.

[10] R. M. Nadeau and L. R. Johnson, "Seismological studies at parkfield vi; moment release rates and estimates of source parameters for small repeating earthquakes," eng, *Bulletin of the Seismological Society of America*, vol. 88, no. 3, pp. 790–814, 1998, ISSN: 0037-1106. DOI: https://doi.org/10.1785/BSSA0880030790.

[11] S. D. Goodfellow and R. P. Young, "A laboratory acoustic emission experiment under in situ conditions," *Geophysical Research Letters*, vol. 41, pp. 3422–3430, 10 2014, ISSN: 19448007. DOI: 10.1002/2014GL059965.

[12] L. Malagnini, K. Mayeda, S. Nielsen, *et al.*, "Scaling transition in earthquake sources: A possible link between seismic and laboratory measurements," eng, *Pure and applied geophysics*, vol. 171, no. 10, pp. 2685–2707, 2013, ISSN: 0033-4553. DOI: https://doi.org/10.1007/s00024-013-0749-8.

[13] G. Di Toro, R. Han, T. Hirose, *et al.*, "Fault lubrication during earthquakes," eng, *Nature*, vol. 471, no. 7339, pp. 494–498, 2011, ISSN: 0028-0836. DOI: https://doi.org/10.1038/nature09838.

[14] S. Ide and G. C. Beroza, "Does apparent stress vary with earthquake size?" *Geophysical Research Letters*, vol. 28, no. 17, pp. 3349–3352, 2001. DOI: https://doi.org/10.1029/2001GL013106. eprint: https://agupubs.onlinelibrary.wiley.com/doi/pdf/10.1029/2001GL013106. [Online]. Available: https://agupubs.onlinelibrary.wiley.com/doi/abs/10.1029/2001GL013106.

[15] S. Ide, G. C. Beroza, S. G. Prejean, and W. L. Ellsworth, "Apparent break in earthquake scaling due to path and site effects on deep borehole recordings," *Journal of Geophysical Research: Solid Earth*, vol. 108, no. B5, 2003. DOI: https://doi.org/10.1029/2001JB001617. eprint: https://agupubs.onlinelibrary.wiley.com/doi/pdf/10.1029/2001JB001617. [Online]. Available: https://agupubs.onlinelibrary.wiley.com/doi/abs/10.1029/2001JB001617.

[16] G. C. McLaskey and S. D. Glaser, "Hertzian impact: Experimental study of the force pulse and resulting stress waves," *The Journal of the Acoustical Society of America*, vol. 128, p. 1087, 3 2010, ISSN: 00021369. DOI: 10.1080/00021369.1990.10869910. [Online]. Available: http://scitation.aip.org/content/asa/journal/jasa/128/3/10.1121/1.3466847.

[17] G. C. McLaskey and S. D. Glaser, "Micromechanics of asperity rupture during laboratory stick slip experiments," *Geophysical Research Letters*, vol. 38, pp. 1–5, 12 2011. DOI: 10.1029/2011GL047507.

[18] G. C. McLaskey, B. D. Kilgore, D. A. Lockner, and N. M. Beeler, "Laboratory generated m -6 earthquakes," *Pure and Applied Geophysics*, vol. 171, pp. 2601–2615, 10 2014, ISSN: 14209136. DOI: 10.1007/s00024-013-0772-9.

[19] P. A. Selvadurai and S. D. Glaser, "Novel monitoring techniques for characterizing frictional interfaces in the laboratory," *Sensors (Switzerland)*, vol. 15, pp. 9791–9814, 5 2015, ISSN: 14248220. DOI: 10.3390/s150509791.

[20] P. A. Selvadurai and S. D. Glaser, "Laboratory-developed contact models controlling instability on frictional faults," *Journal of Geophysical Research: Solid Earth*, vol. 120, no. 6, pp. 4208–4236, 2015. DOI: https://doi.org/10.1002/2014JB011690. [Online]. Available: https://agupubs.onlinelibrary.wiley.com/doi/abs/10.1002/2014JB011690.

[21] S. E. Minson and D. S. Dreger, "Stable inversions for complete moment tensors," *Geophysical Journal International*, vol. 174, pp. 585–592, 2 Aug. 2008, ISSN: 1365-246X. DOI: 10.1111/J.1365-246X.2008.03797.X.

[22] G. C. McLaskey and S. D. Glaser, "Acoustic emission sensor calibration for absolute source measurements," *Journal of Nondestructive Evaluation*, vol. 31, pp. 157–168, 2 2012, ISSN: 01959298. DOI: 10.1007/s10921-012-0131-2.

[23] G. Kwiatek, T. H. Goebel, and G. Dresen, "Seismic moment tensor and b value variations over successive seismic cycles in laboratory stick-slip experiments," *Geophysical Research Letters*, vol. 41, pp. 5838–5846, 16 2014, ISSN: 19448007. DOI: 10.1002/2014GL060159.

[24] E. Stierle, V. Vavryčuk, G. Kwiatek, E.-M. Charalampidou, and M. Bohnhoff, "Seismic moment tensors of acoustic emissions recorded during laboratory rock deformation experiments: Sensitivity to attenuation and anisotropy," eng, *Geophysical journal international*, vol. 205, no. 1, pp. 38–50, 2016, ISSN: 0956-540X. DOI: https://doi.org/10.1093/gji/ggw009.

[25] P. A. Selvadurai, "Laboratory studies of frictional sliding and the implications of precursory seismicity," Ph.D. dissertation, University of California, Berkeley, 2015.

[26] N. N. Hsu, *Dynamic green's functions of an infinite plate - a computer program*, eng, ser. NBSIR ; 85-3234. Gaithersburg, MD: U.S. Dept. of Commerce, National Institute of Standards and Technology, 1985.

[27] R. B. Herrmann, "Computer programs in seismology: An evolving tool for instruction and research," *Seismological Research Letters*, vol. 84, pp. 1081–1088, 6 Nov. 2013, ISSN: 08950695. DOI: 10.1785/0220110096.

[28] B. Romanowicz and B. Mitchell, "1.21 - deep earth structure – q of the earth from crust to core," in *Treatise on Geophysics*, G. Schubert, Ed., Amsterdam: Elsevier, 2007, pp. 731–774, ISBN: 978-0-444-52748-6. DOI: https://doi.org/10.1016/B978-044452748-6.00024-9. [Online]. Available: https://www.sciencedirect.com/science/article/pii/B9780444527486000249.

[29] R. Kono, "The dynamic bulk viscosity of polystyrene and polymethyl methacrylate," *Journal of the Physical Society of Japan*, vol. 15, no. 4, pp. 718–725, 1960. DOI: 10.1143/JPSJ.15.718. eprint: https://doi.org/10.1143/JPSJ.15.718. [Online]. Available: https://doi.org/10.1143/JPSJ.15.718.

[30] K. Aki and P. G. Richards, *Quantitative Seismology*, 2nd. University Science Books, 2002.

[31] A. C. To and S. D. Glaser, "Full waveform inversion of a 3-d source inside an artificial rock," eng, *Journal of sound and vibration*, vol. 285, no. 4, pp. 835–857, 2005, ISSN: 0022-460X. DOI: https://doi.org/10.1016/j.jsv.2004.09.001.

[32] L. Krischer, T. Megies, R. Barsch, *et al.*, "Obspy: A bridge for seismology into the scientific python ecosystem," eng, *Computational science & discovery*, vol. 8, no. 1, pp. 14 003–17, 2015, ISSN: 1749-4699. DOI: https://doi.org/10.1088/1749-4699/8/1/014003.

[33] O. S. Boyd, D. S. Dreger, V. H. Lai, and R. Gritto, "A Systematic Analysis of Seismic Moment Tensor at The Geysers Geothermal Field, California," *Bulletin of the Seismological Society of America*, vol. 105, no. 6, pp. 2969–2986, Nov. 2015, ISSN: 0037-1106. DOI: 10.1785/0120140285. [Online]. Available: https://doi.org/10.1785/0120140285.

[34] R. Sleeman and T. van Eck, "Robust automatic p-phase picking: An on-line implementation in the analysis of broadband seismogram recordings," *Physics of the Earth and Planetary Interiors*, vol. 113, pp. 265–275, 1999. DOI: https://doi.org/10.1016/S0031-9201(99)00007-2.

[35] P. Virtanen, R. Gommers, T. E. Oliphant, *et al.*, "SciPy 1.0: Fundamental Algorithms for Scientific Computing in Python," *Nature Methods*, vol. 17, pp. 261–272, 2020. DOI: 10.1038/s41592-019-0686-2.

[36] N. Maeda, "A method for reading and checking phase time in auto-processing system of seismic wave data," jpn ; eng, *Jisin*, vol. 38, no. 3, pp. 365–379, 1985, ISSN: 0037-1114. DOI: https://doi.org/10.4294/zisin1948.38.3_365.

[37] A. K. Yadav and P. K. Mishra, "Method for detection of first phase in seismogram based on akaike information criterion (aic) function," *International journal of engineering research and technology*, vol. 3, 2014, ISSN: 2278-0181.

[38] N. A. Haskell, "Radiation Pattern of Rayleigh Waves from A Fault of Arbitrary Dip and Direction of Motion in a Homogeneous Medium," *Seismological Research Letters*, vol. 33, no. 4, pp. 71–87, Dec. 1962, ISSN: 0895-0695. DOI: 10.1785/gssrl.33.4.71. eprint: https://pubs.geoscienceworld.org/ssa/srl/article-pdf/33/4/71/2751098/71.pdf. [Online]. Available: https://doi.org/10.1785/gssrl.33.4.71.

[39] T. Lay and T. Wallace, *Modern global seismology*, eng, ser. International geophysics series ; v. 58. San Diego: Academic Press Elsevier, 1995, ISBN: 9780080536712.

[40] R. Madariaga, "Dynamics of an expanding circular fault," *Bulletin of the Seismological Society of America*, vol. 66, no. 3, pp. 639–666, Jun. 1976, ISSN: 0037-1106. DOI: 10.1785/BSSA0660030639. eprint: https://pubs.geoscienceworld.org/ssa/bssa/article-pdf/66/3/639/5320365/bssa0660030639.pdf. [Online]. Available: https://doi.org/10.1785/BSSA0660030639.

[41] Z. E. Ross, M.-A. Meier, E. Hauksson, and T. H. Heaton, "Generalized seismic phase detection with deep learning," eng, *Bulletin of the Seismological Society of America*, vol. 108, no. 5A, pp. 2894–2901, 2018, ISSN: 0037-1106. DOI: https://doi.org/10.1785/0120180080.

[42] P. Shi, F. Grigoli, F. Lanza, G. C. Beroza, L. Scarabello, and S. Wiemer, "MALMI: An Automated Earthquake Detection and Location Workflow Based on Machine Learning and Waveform Migration," *Seismological Research Letters*, May 2022, ISSN: 0895-0695. DOI: 10.1785/0220220071. eprint: https://pubs.geoscienceworld.org/ssa/srl/article-pdf/doi/10.1785/0220220071/5602568/srl-2022071.1.pdf. [Online]. Available: https://doi.org/10.1785/0220220071.

[43] T. Candela and E. E. Brodsky, "The minimum scale of grooving on faults," eng, *Geology (Boulder)*, vol. 44, no. 8, pp. 603–606, 2016, ISSN: 0091-7613. DOI: https://doi.org/10.1130/G37934.1.

[44] E. E. Brodsky, J. D. Kirkpatrick, and T. Candela, "Constraints from fault roughness on the scale-dependent strength of rocks," eng, *Geology (Boulder)*, vol. 44, no. 1, pp. 19–22, 2016, ISSN: 0091-7613. DOI: https://doi.org/10.1130/G37206.1.